https://doi.org/10.5194/gmd-2023-207
Preprint. Discussion started: 22 November 2023

Geoscientific Model Development Discussions

Assessment of a multi-tiling energy budget approach in a land surface model, ORCHIDEE-MICT (r8205)

Yi Xi[1], Chunjing Qiu[2,3], Yuan Zhang[4,1], Dan Zhu[5], Shushi Peng[5], Gustaf Hugelius[6], Jinfeng Chang[7], Elodie Salmon[1], Philippe Ciais[1]

[1]Laboratoire des Sciences du Climat et de l'Environnement, LSCE/IPSL, CEA – CNRS – UVSQ, Université Paris-Saclay, 91191 Gif-sur-Yvette, France
[2]Research Center for Global Change and Complex Ecosystems, School of Ecological and Environmental Sciences, East China Normal University, Shanghai, China.
[3]Institute of Eco-Chongming, East China Normal University, Shanghai, China
[4]Key Laboratory of Alpine Ecology, Institute of Tibetan Plateau Research, Chinese Academy of Sciences, Beijing 100101, China;
[5]Sino-French Institute for Earth System Science, College of Urban and Environmental Sciences, Peking University, Beijing 100871, China
[6]Department of Physical Geography, Stockholm University, Stockholm, Sweden
[7]College of Environmental and Resource Sciences, Zhejiang University, Hangzhou, China

Correspondence to: Yi Xi (yi.xi@lsce.ipsl.fr)

Abstract. The surface energy budget plays a critical role in terrestrial hydrologic and biogeochemical cycles. Nevertheless, its highly spatial heterogeneity across different vegetation types is still missing in the land surface model, ORCHIDEE-MICT (ORganizing Carbon and Hydrology in Dynamic EcosystEms–aMeliorated Interactions between Carbon and Temperature). In this study, we describe the representation of a multi-tiling energy budget in ORCHIDEE-MICT, and assess its short and long-term impacts on energy, hydrology, and carbon processes. With the specific values of surface properties for each vegetation type, the new version presents warmer surface and soil temperatures, wetter soil moisture, and increased soil organic carbon storage across the Northern Hemisphere. Despite reproducing the absolute values and spatial gradients of surface and soil temperatures from satellite and in-situ observations, the considerable uncertainties in simulated soil organic carbon and hydrologic processes prevent an obvious improvement of temperature bias existing in the original ORCHIDEE-MICT. However, the separation of sub-grid energy budgets in the new version improves permafrost simulation greatly by accounting for the presence of discontinuous permafrost type, which will facilitate various permafrost-related studies in the future.

https://doi.org/10.5194/gmd-2023-207
Preprint. Discussion started: 22 November 2023

Geoscientific Model Development Discussions

1 Introduction

The surface energy balance is a fundamental component of the Earth system. The incoming solar energy is not only essential for life and plant photosynthesis but also drives the terrestrial hydrologic cycle (i.e., evapotranspiration and the freeze-thaw cycle of soils in cold regions) and modulates the speed of biogeochemical reactions (i.e., the decomposition of organic matter). The energy balance depends on landscape type through distinct vegetation and soil elements which reflect and emit shortwave and longwave electromagnetic radiation in different proportions. Understanding and simulating the complex interactions of energy, hydrology, and biogeochemical processes throughout the Earth system is crucial for tracking the consequences of historical human activities and predicting the future of our Earth's climate system.

Temperature at the surface (T_{surf}) is an important indicator of energy transfer from the atmosphere to the ecosystem. Two adjacent landscapes could have significantly different T_{surf} due to their distinct surface properties. For instance, a higher albedo across snow-covered areas for short vegetation compared to forest would result in a reduction in the absorbed solar energy and lower the T_{surf}, with a magnitude depending on the timing and duration of snow cover (Zhang, 2005). The larger water storage in wetlands (with a high specific heat capacity of water) against adjacent upland land cover types would warm or cool the surface by approximately 1 °C by regulating the seasonality of ground heat flux (Wu et al., 2021). The larger latent heat loss via evapotranspiration over deep rooted tropical forests compared to nearby grassland and cropland show a significant cooling effect, approximately -2.5 °C on a daily basis (Li et al., 2015). Such a substantial T_{surf} difference would not only lead to the difference in biophysical and biogeochemical processes at the surface, but also propagate downward and differentiate the temperature in the soil (T_{soil}) and subsequent soil biophysics and biogeochemistry among various adjacent landscapes. Recently, most land surface models (LSMs) have introduced multi-tiling energy budgets to completely or partly represent sub-grid scale heterogeneity of surface energy exchange, for example, the separate energy budgets for snow, soil, and vegetation in ISBA (the Soil–Biosphere–Atmosphere LSM) (Boone et al., 2017), the partition of snow-cover and snow-free land units in CLM 5.0 (the Community Land Model) (Lawrence et al., 2019), the surface–soil tiling scheme for the land surface model JULES (the Joint UK Land Environment Simulator) (Rumbold et al., 2023). Compared to the "composite" simulation (using the average of vegetation attributes within a grid cell), the "mosaic" simulation (using specific attributes of different vegetation types for water and energy balance) using the CLASSIC model estimated a 19% higher terrestrial carbon sink for 1959-2005 (Melton and Arora, 2014; Melton et al., 2020). Despite the potential uncertainties in models-specific structure and configuration, such a significantly different estimation of the global land carbon sink highlights the importance of representing the spatial heterogeneity of sub-grids in simulating terrestrial energy and water balance.

In this study, we present a new representation of multi-tiling energy budget at the surface and subsurface for each plant function type (PFT) in a state-of-the-art LSM, ORCHIDEE-MICT (ORganizing Carbon and Hydrology in Dynamic EcosystEms–aMeliorated Interactions between Carbon and Temperature), which calculates turbulent fluxes for subgrid PFT

https://doi.org/10.5194/gmd-2023-207
Preprint. Discussion started: 22 November 2023


Geoscientific Model Development Discussions

types but solves for an average grid-level energy budget resulting into a single surface temperature (Guimberteau et al., 2018). Some hydrologic and biogeochemical processes in the model have been modified correspondingly to include PFT-specific thermal inputs. In Sect. 2, we provide a brief review of the current single-tiling energy budget at surface and subsurface, while Sect. 3 describes the modifications made to implement the multi-tiling energy budget in the model. To evaluate the impacts of separating the energy budget for each PFT on the energy, hydrology, soil thermics and carbon cycles, we conduct simulations using the original version of ORCHIDEE-MICT (referred to as MICT) and the new multi-tiling energy budget version (referred to as MICT-teb) as described in Sect. 4. The results of these simulations are compared in Sect. 5. Section 6 focuses on the evaluation of energy processes in the new version as well as the improvements for permafrost simulations. Finally, we present conclusions in Sect. 7.

2 Overview of current energy budget in ORCHIDEE-MICT

ORCHIDEE-MICT is a branch of the ORCHIDEE model (Krinner et al., 2005) specifically developed to enhance the representation of hydrologic and biogeochemical interactions in high latitude regions (Guimberteau et al., 2018). In comparison to the trunk version 3976 from which it was developed, ORCHIDEE-MICT includes several key new processes, namely 1) the feedback effects of soil organic carbon (SOC) concentration on soil thermal and soil water dynamics (Zhu et al., 2019); 2) soil carbon vertical discretization (Koven et al., 2009; Zhu et al., 2016); 3) vertical mixing of soil carbon due to cryoturbation (in cold soils) and bioturbation (Koven et al., 2009, 2013); 4) reformulation of soil hydric stress above the permafrost table (Zhu et al., 2015); 5) the inclusion of northern peatlands as a specific PFT with peatland-specific hydrology, carbon decomposition and accumulation (Qiu et al., 2018, 2019). These new processes have significantly improved the representation of plant productivity, water cycle, soil carbon stocks, and the simulated permafrost distribution in high latitude regions, but there is still room for improvement (Guimberteau et al., 2018). One important aspect that calls for attention is the need to include sub-grid representations of surface and subsurface energy budgets, especially in the high latitudes where snow cover and water equivalent differs between PFTs, and where soil carbon differences across landscape elements / PFTs within the same grid-cell results into heterogeneous soil temperature and active layer thickness. For the moment, within the ORCHIDEE-MICT model, there are three major modules: carbon, water, and energy. The carbon cycle module operates for each PFT sub-grid and the water cycle operates for each soil tile (divided into bare soil, tree PFTs, grass and crop PFTs, and peatland PFT categories), while the energy module is solved only at the total grid-cell level (Best et al., 2004). Figure 1 shows the schematic representation of energy budgets from the surface to snow and soil layers in the original and new versions of ORCHIDEE-MICT, namely MICT and MICT-teb. The details of the energy budget in the model are described as follows.

https://doi.org/10.5194/gmd-2023-207
Preprint. Discussion started: 22 November 2023

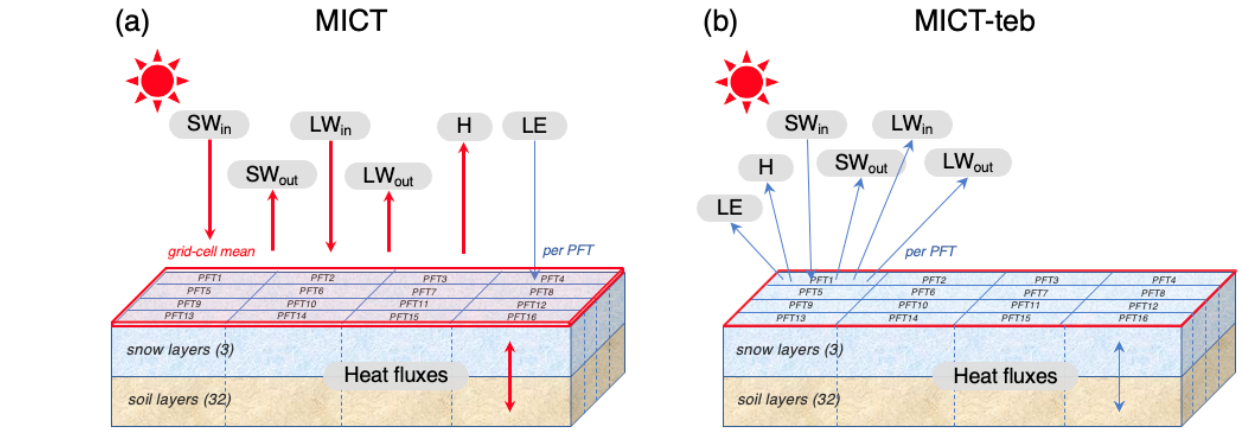

Figure 1: An example for accurate data representation & universal readability of figures. Figure 1. Schematic representation of energy budgets at the surface, snow layers, and soil layers in ORCHIDEE-MICT (MICT) (a) and the new multi-tiling energy budget version (MICT-teb) (b). SW_{in}, SW_{out}, LW_{in}, LW_{out}, H, and, LE represent incoming ShortWave radiation, outward ShortWave radiation, incoming LongWave radiation, outward LongWave radiation, sensible heat flux, latent heat flux, respectively. PFT indicates Plant Function Type. There are 3 layers for snow, and 32 layers for soil in the model. In MICT, SW_{in}, SW_{out}, LW_{in}, LW_{out}, H, and heat fluxes in snow and soil layers are calculated as grid-cell mean but LE is calculated for each PFT, while in MICT-teb, all of the heat fluxes are calculated for each PFT.

2.1 Surface energy budgets

Similar to most LSMs, the surface energy budget equation is used in MICT to describe the balance of net absorbed radiation (R_{net}) by the energy transferred out of the ecosystem:

$$R_{net} = H + LE + G + \Delta S \quad (1)$$

where H is sensible heat flux (W m^{-2}); LE is latent heat flux (W m^{-2}); G is ground heat flux (W m^{-2}); ΔS is the energy stored in the ecosystem as chemical energy through photosynthesis and as the temperature change of the plant biomass (W m^{-2}). Due to the ΔS only accounting for < 5% of total energy budget of the ecosystem, it is neglected in the model. R_{net} is the balance of the inputs and outputs of shortwave radiation (SW_{in} and SW_{out}) and longwave radiation (LW_{in} and LW_{out}):

$$R_{net} = (SW_{in} - SW_{out}) + (LW_{in} - LW_{out}) = (1 - \alpha) \times SW_{in} + \left(LW_{in} - \sigma \times \varepsilon \times (T_{surf})^4\right) \quad (2)$$

where α is the albedo which determines the proportion of incoming SW absorbed by the ecosystem (unitless); σ is Stefan-Boltzman constant (5.6697×10^{-8} W m^{-2} K^{-4}); ε is emissivity (1, unitless) and T_{surf} is the surface temperature at grid scale (K). In MICT, the grid-cell α is calculated as the area-weighted average of the α across all PFTs. The snow-covered areas and snow-free areas are distinguished in terms of the higher albedo of snow than canopy and bare soil (see details in Sect. 2.3). The albedo of bare soil in the current version is prescribed using static satellite observations (Boucher et al., 2020), thus without interannual variations and decoupled with simulated soil moisture (Fig. S1). For the three heat fluxes out of the surface, the H and LE are calculated following Eqs. (3) and (4), respectively:

https://doi.org/10.5194/gmd-2023-207
Preprint. Discussion started: 22 November 2023

Geoscientific Model Development Discussions

$$H = \rho \times v \times C_d \times C_p \times (T_{surf} - T_{air}) \quad (3)$$

$$LE = L \times \beta \times \rho \times v \times C_d \times (q_{surf} - q_{air}) \quad (4)$$

where ρ is air density (kg m^{-3}); v is horizontal wind speed (m s^{-1}); C_d is drag coefficient (unitless); C_p is the specific heat of dry air (1004.675 J kg^{-1} K^{-1}); T_{air} is the air temperature (K); L is the latent heat of evaporation or sublimation (2.5008 or 2.8345 × 10^6 J kg^{-1}); β is the limiting factor of potential total evapotranspiration (PET) (unitless); q_{surf} and q_{air} are the saturated moisture at the surface and in the air (kg kg^{-1}), respectively. Due to the differences in canopy height and leaf area index (LAI), C_d should be different among different PFTs. To ensure compatibility with the grid-cell calculation of surface energy budget, the C_d of different PFTs is weighted by their area. The LE (or ET) serves as the link between the energy cycle and hydrologic and carbon cycle. It is PFT-specific via a PFT-specific β (see details in Ducharne, 2018) because the carbon cycle and hydrologic processes separate different PFTs or different soil tiles. In MICT, the LE consists of E_{flood} (flood evaporation, not activated in the simulations of this study), E_{subli} (snow sublimation), E_{soil} (evaporation from bare soil), E_{trans} (transpiration), and E_{inter} (interception). Due to the distinct plant structures between different PFTs, the evaporation components associated with vegetation, i.e. E_{trans} and E_{inter} are PFT-specific, while the E_{subli} and E_{soil} are calculated as the grid-cell average. For G, the energy exchange between surface and ground (snow or soil depending on the snow cover fraction), it is calculated following the classic Fourier's law (Hourdin, 1992). Considering that the calculation of G is identical to heat conduction in soil layers, the detailed derivation is only shown in Sect. 2.2 to avoid redundancy. For the areas covered by snow, the G also considers heat fluxes into snowpack which are used to melt snow.

2.2 Soil energy budgets

Table S1 displays the vertical discretization of soil in the current version of MICT. There are 32 soil layers for soil heat conduction with a total depth of 38 m and 11 soil layers for soil hydrology with a total depth of 2 m. These soil layers are located below the three snow layers in the model when there is snow (Fig. 1 (a)). As mentioned earlier, the heat conduction across soil layers, snow layers, and between the surface and ground is calculated using the classic one-dimension Fourier's law (Hourdin, 1992), with the latent flux of soil-freezing into consideration (Gouttevin et al., 2012):

$$c\frac{\partial T_{soil}}{\partial t} = \frac{\partial}{\partial z}\left(\lambda\frac{\partial T_{soil}}{\partial z}\right) + \rho_{ice} L \frac{\partial \theta_{ice}}{\partial t} \quad (5)$$

where c is volumetric soil heat capacity (J K^{-1} m^{-3}); T_{soil} is the soil temperature (K); λ is the soil thermal conductivity (J m^{-1} s^{-1} K^{-1}); ρ_{ice} is ice density (920 kg m^{-3}); L is latent heat of fusion (0.3336 × 10^6 J kg^{-1}); θ_{ice} is volumetric ice content (m^3 m^{-3}); t is time (s) and z is soil layer depth (m). The c is calculated as the area-weighted sum of the heat capacity of liquid soil moisture (4.18 × 10^6 J K^{-1} m^{-3}), frozen soil moisture (2.11 × 10^6 J K^{-1} m^{-3}), and soil (depending on the soil type and the SOC content). The λ is calculated following:

$$\lambda = Ke \times \lambda_{sat} + (1 - Ke) \times \lambda_{dry} \quad (6)$$

https://doi.org/10.5194/gmd-2023-207
Preprint. Discussion started: 22 November 2023


Geoscientific Model Development Discussions

with

$$\lambda_{sat} = \lambda_{solid}^{(1-\theta_{sat})} + \lambda_{liq}^{\left(\theta_{sat}\times\frac{\theta_{liq}}{\theta_{liq}+\theta_{ice}}\right)} + \lambda_{ice}^{\left(\theta_{sat}\times\frac{\theta_{ice}}{\theta_{liq}+\theta_{ice}}\right)} \quad (7)$$

where Ke is Kersten number calculated using a function of soil moisture saturated degree; λ_{sat} and λ_{dry} are the saturated and dry thermal conductivities (W m^{-1} k^{-1}), respectively; θ_{sat} is saturated soil moisture, depending on the soil type and the SOC content (m^3 m^{-3}); θ_{liq} is volumetric liquid water content (m^3 m^{-3}); λ_{solid} is the thermal conductivity of soil solid material, calculated as the geometric mean conductivities of mineral soil and SOC; λ_{liq} and λ_{ice} are the thermal conductivities of water (0.57 W m^{-1} k^{-1}) and ice (2.2 W m^{-1} k^{-1}), respectively. The two thermal parameters are calculated for each soil layer because the heat is transferred vertically across all soil layers. The input liquid or frozen soil moisture (SM) are calculated as the area-weighted sum of all soil tiles to keep consistency with the grid-cell energy budget, despite the fact that soil hydrology and soil carbon processes operate for each sub-grid element (soil tile for hydrology or PFT for carbon).

2.3 Snow energy budgets

An explicit snow model of intermediate complexity has been introduced in MICT as described in Wang et al. (2013). The snowpack includes three snow layers (Fig. 1), with snow settling, water percolation, and refreezing and thawing of snow taken into account. When evaluated against observation data, the new snow module has improved the heat interaction between snow and soil or ground surface (Wang et al., 2013). The heat conduction in snow layers uses the same one-dimension heat diffusion function as that in soil layers (Eq. (5)), while with the snow's heat capacity (c_{snow}) and thermal conductivity (λ_{snow}):

$$c_{snow} = \rho_{snow} \times c_{p\_ice} \quad (8)$$

$$\lambda_{snow} = \left(a_\lambda + b_\lambda \times (\rho_{snow})^2\right) + \left(a_{\lambda v} + \frac{b_{\lambda v}}{T_{snow} - c_{\lambda v}}\right) \times \frac{P_0}{P_a} \quad (9)$$

where ρ_{snow} is snow density (kg m^{-3}), varying with the snow settling; c_{p_ice} is the heat capacity of ice (2.11 × 10^6 J K^{-1} m^{-3}); the parameters a_λ = 0.02, b_λ = 2.50 × 10^{-6}, $a_{\lambda v}$ = -0.06, $b_{\lambda v}$ = -2.54, $c_{\lambda v}$ = -289.99, P_0 = 1000 hPa; T_{snow} is the temperature of snow layers; and P_a is atmospheric pressure (hPa). Besides the two thermal parameters, snow albedo (α_{snow}) is a key variable affecting the surface energy budget (Wang et al., 2013). The value of α_{snow} is calculated following:

$$\alpha_{snow} = \alpha_{snow\_min} + k \times e^{\left(-\frac{age_{snow}}{\tau}\right)} \quad (10)$$

where α_{snow_min} is the minimum snow albedo value after aging; k is the decay rate of snow albedo; age_{snow} is the snow age; and τ is the time constant of the decay of snow albedo (10 days). Although α_{snow_min} and k vary across different vegetation types (Table S2), the α_{snow} and all other snow-related processes including the heat conduction across the snow layers are still calculated at grid-cell scale by weighted area in MICT.

https://doi.org/10.5194/gmd-2023-207
Preprint. Discussion started: 22 November 2023

Geoscientific Model Development Discussions

3 Implementation of multi-tiling energy budget in ORCHIDEE-MICT-teb

To represent the sub-grid energy budget in MICT, we calculate PFT-specific surface properties including the roughness height and the albedo of different PFTs to start the separation of surface energy budgets for each PFT, and then add the PFT-specific calculation for energy budget at the surface as well as in snow and soil layers (Figs. 1 and 2). Owing to using distinct input variables from the energy budget module, some processes in the hydrology cycle and carbon cycle are also modified correspondingly. The details of all of the modifications are described as follows.

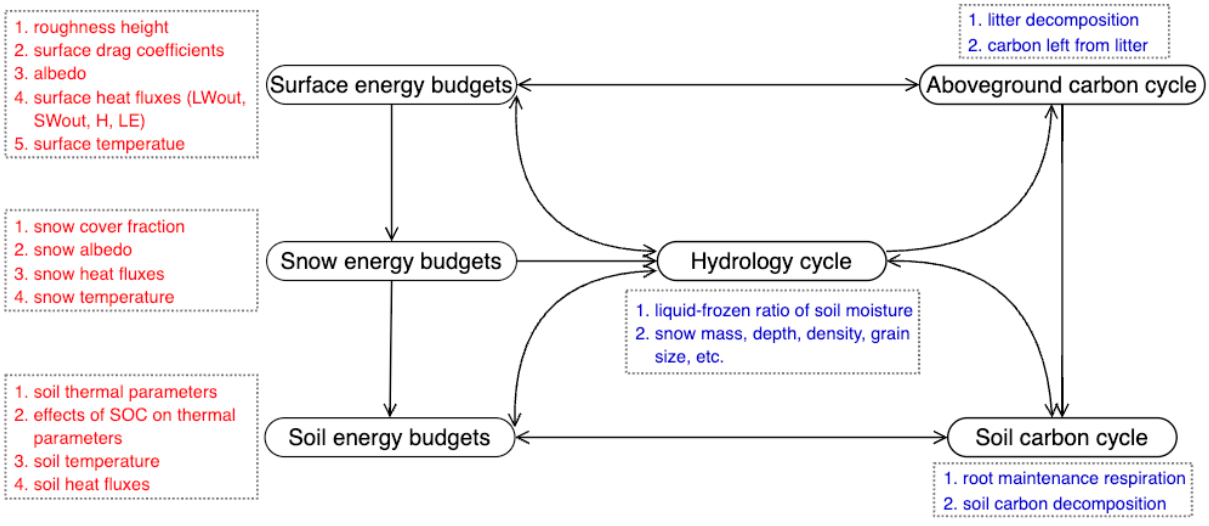

Figure 2: Modifications of energy, hydrology, and carbon processes to implement multi-tiling energy budgets in ORCHIDEE-MICT in this study. The black rounded rectangles show the main modules in ORCHIDEE-MICT, and the red or blue sharp rectangles show the processes which are modified to include the multi-tilling energy budget. The red and blue here distinct the processes where the PFT-specific calculations are added actively and those modified passively due to the input variables changing following the multi-tilling surface, snow, and soil thermics.

3.1 Surface energy budgets

Differences in surface properties serve as the foundation for distinct surface energy budgets across sub-grids. For example, variations in vegetation heights among tree, grass, and bare soil result in different aerodynamic roughness, then drag coefficients, and then different turbulent fluxes including H and LE (Eqs. (3) and (4)). Different surface types among tree, grass, and bare soil also result in different surface albedo (α), influencing the amount of solar radiation reflected by the surface (Eq. (2)). In MICT-teb, we employ the specific roughness height (H_{rough}, vegetation height minus zero plane displacement height) and albedo for each PFT (Tables S2-S4 and Fig. S1), instead of the average values of all PFTs within a

https://doi.org/10.5194/gmd-2023-207
Preprint. Discussion started: 22 November 2023


Geoscientific Model Development Discussions

grid-cell used in MICT. That means, if only considering the changes in surface properties, the more heterogeneous the subgrid PFT distribution is, the larger differences in the energy and the subsequent hydrology and carbon-related processes between MICT-teb and MICT may be. The distinct surface properties among different PFTs propagate to differences in surface energy fluxes and then differentiate the T_{surf} across different PFTs. In MICT-teb, all processes related to the changes in surface properties and T_{surf} in the surface energy budget are separated and operate independently for each PFT (Fig. 2).

For LE (or ET), it comprises four components: E_{subli}, E_{soil}, E_{trans}, and E_{inter} in the model. As described in Sect. 2.1, only E_{trans} and E_{inter} are PFT-specific in the original MICT. However, due to the modifications made to surface energy budgets and surface properties resulting in varying snow cover fractions across different PFTs, E_{subli} is now separated for each PFT in MICT-teb. Regarding E_{soil}, the water limitation in the hydrology module differs among different soil tiles, whereas in MICT, it is considered at grid scale only. The calculation of E_{soil} has been modified by using the specific water limitation for each soil tile in MICT-teb. All PFTs in one soil tile are distributed the same value of E_{soil}, and then are used in PFT-specific calculation in energy modules.

3.2 Snow energy budgets

The modifications to the surface energy budget in MICT-teb, which cause variations in heat fluxes into the snowpack, result in differences in the formation and melting of snow and then snow mass, snow depth (dz_{snow}), and snow density (ρ_{snow}) among different PFTs. The snow cover fraction (f_{snow}) as calculated in MICT following:

$$f_{snow} = tanh(\sum_{i=1}^{3}(dz_{snow,i})/0.025 * (\sum_{i=1}^{3}(dz_{snow,i} * \rho_{snow,i}) / \sum_{i=1}^{3}(dz_{snow,i}))/50) \quad (11)$$

would be different among different PFTs, where i is the index of snow layer. The variations in f_{snow} would subsequently influence the surface albedo due to snow (Eq. (10)) and, in turn, the snow feedbacks on the surface energy budget. All of the snow-related processes have been separated for each PFT in MICT-teb (Fig. 2).

3.3 Soil energy budgets

Following Eq. (5), modifications of energy budgets at surface and in snow layers could result in variations in the starting point of heat conduction in soil for different PFTs. While within soil, the heat conduction is more regulated by the heat capacity (c) and thermal conductivity (λ). Liquid SM, frozen SM, and SOC are three key factors influencing the two thermal parameters in the model (Eqs. (6) and (7)). In the original MICT, the average values of these three factors across all PFTs are used due to the limitation of having a grid-scale mean energy budget. In the new version, we simulate PFT-specific liquid SM and frozen SM in energy modules to represent the heterogeneity of different PFTs, following the separation of soil heat conduction (Fig. 2). Regarding SOC, MICT uses the grid-cell SOC obtained from an observation-based SOC map (FAO,

https://doi.org/10.5194/gmd-2023-207
Preprint. Discussion started: 22 November 2023


Geoscientific Model Development Discussions

2012; Zhu et al., 2019; Guimberteau et al., 2018; Hugelius et al., 2013) and therefore the effects of SOC on thermal parameters are represented homogeneously within each grid cell. According to Zhu et al. (2019), an increase of 20 kg C m^{-3} in SOC between two PFTs, which can be found in site-level data (Palmtag et al., 2022) and is reproduced in model simulations (Fig. S2), could result in a 42-52% decrease in thermal diffusivity (λ/c) and a subsequent 13-18% increase in current permafrost extent. The important role of SOC in regulating soil thermal regimes and the heterogeneity of SOC across different PFTs highlight the pressing need to represent the thermal effects of SOC for each sub-grid. However, limited by the availability of observed SOC data that could be prescribed for sub-grids at the regional or global scale, we utilize the simulated SOC for each PFT in MICT-teb and the simulated total SOC of all PFTs in MICT. Using simulated instead of prescribed SOC has the advantage of making the modeled SOC fully consistent with the simulated soil physics, but it has the drawback that SOC formed by processes that cannot be simulated by the model (e.g. pleistocene ecosystems such as Yedoma, thermokarst lakes filling by organic sediments) will be ignored, causing a possible mismatch with observed SOC density. Nevertheless, a comparable spatial pattern of gridded SOC for 0-3 m over the Northern Hemisphere (NH) against observation-based SOC data, as well as a comparable vertical profile against site-level data (Palmtag et al., 2022), confirm the model's ability to simulate the total volume (Fig. S3) and the PFT-specific vertical profiles (Fig. S2) of SOC.

3.4 Associated modifications of hydrological and carbon processes

Soil temperature (T_{soil}) is a key factor to influence hydrologic and biogeochemical processes in soil. Therefore, the PFT-specific variations in T_{soil} result in a series of associated modifications of hydrological and carbon-related processes in relation to the original MICT (Fig. 2). For soil hydrology, there are three main modifications in MICT-teb compared to MICT: 1) the calculation of PFT-specific T_{soil} for each PFT to calculate liquid-frozen ratio of SM; 2) the use of PFT-specific bare soil evaporation from the energy module; and 3) the separation of snow-related processes for each PFT. For the soil carbon cycle, there are four main modifications in MICT-teb: 1) the use of PFT-specific T_{soil} and SM for litter decomposition; 2) the use of PFT-specific T_{soil} and SM to calculate carbon flow from litter to soil; 3) the use of PFT-specific T_{soil} and SM for root maintenance respiration; and 4) the use of PFT-specific T_{soil} and SM for soil carbon decomposition.

4 Simulation protocol and forcing datasets

To compare the differences in energy, hydrology, and carbon processes between MICT-teb and MICT, we design three groups of simulations (S0, S1, and S2) as shown in Table 1. All of the three groups are run for the NH (0°-90°N) at a spatial resolution of 2° × 2°, with three simulation periods: A) Spin-up1, 100 years of the full ORCHIDEE with a looped 1901-1920 climate, CO_2 level of 1901 at 296.80 ppm, and the land cover map of 1901; B) SubC, 10,000 years of the soil carbon sub-model (offline) to accumulate SOC; C) Spin-up2, 50 years of the full ORCHIDEE to reach equilibrium with a looped 1901-

https://doi.org/10.5194/gmd-2023-207
Preprint. Discussion started: 22 November 2023

1920 climate, CO_2 level of 1901, and the land cover map of 1901. The climate forcing data are obtained from CRU-JRA v2.3, while the land cover map is generated by combining the land cover map from TRENDY for 15 PFTs (bare soil, 8 tree PFTs, 4 grass PFTs, and 2 crop PFTs) and the peat map from Xu et al. (2018) for the peat grass PFT (Xu et al., 2018; Qiu et al., 2019). In S0, the original MICT is used for all three periods. In S1, MICT-teb is used with the flags controlling the multi-tiling energy budget (MTEB) turned off for periods A and B (i.e., identical to group S0), but turned on for period C. In this way, the differences in energy, hydrology, and carbon between S0 and S1 solely due to the MTEB can be compared based on the same starting point (end of period B). In S2, the flags controlling the MTEB are turned on from the beginning of period A. Thus, comparing S0 and S2 could infer differences in long-term equilibrium of energy and hydrology, as well as near-equilibrium soil carbon storage between MICT-teb and MICT.

Table 1. Simulation protocol. MICT and MICT-teb indicate the original ORCHIDEE-MICT (without tiling energy budget) and the new ORCHIDEE-MICT-teb (with tiling energy budget), respectively. OFF and ON indicate turning off and turning on the flags which control the multi-tiling energy budget in MICT-teb, respectively. If the flags are turned off, all of the PFT-specific variables related to energy budget will use the grid-cell mean value in MICT-teb.

Simulation		S0	S1	S2
Model version		MICT	MICT-teb	MICT-teb
Period	A	√	√ (OFF)	√ (ON)
	B	√	√ (OFF)	√ (ON)
	C	√	√ (ON)	√ (ON)
Notes for the period	A	Spin-up1 (100 yr), Climate: cycle 1901-1920, CO_2: 1901, LUC: 1901		
	B	SubC (10,000 yr)		
	C	Spin-up2 (50 yr), Climate: cycle 1901-1920, CO_2: 1901, LUC: 1901		

5 Evaluation of the impacts of multi-tiling energy budget on energy, hydrology and carbon processes

Following the description of the simulation protocol in Sect. 4, this section presents the differences in energy, hydrology, and carbon processes between MICT-teb and MICT. Sect. 5.1 presents the comparison of S1 and S0, i.e. the impacts solely due to MTEB, while Sect. 5.2 presents the comparison of all the three simulations across the first three simulation periods, i.e. the long-term impacts of MTEB on energy, hydrology, and carbon processes. Unless otherwise stated, all differences indicate the mean values of the last ten years in period C from MICT-teb minus those from MICT in Sect. 5.1.

https://doi.org/10.5194/gmd-2023-207
Preprint. Discussion started: 22 November 2023

Geoscientific Model Development Discussions

5.1 Impacts solely due to multi-tiling energy budget

5.1.1 Surface energy budgets

To explain the differences in energy budgets between MICT-teb and MICT, we begin our analysis by selecting three grid-cells at latitudes for tropical (17ºN, 155ºW), temperate (51ºN, 101ºW) and boreal (71ºN, 147ºE) biomes (Fig. 3). For the energy budgets at surface (Eq. (2)), the SW_{in} and LW_{in} are the same between the two versions (not shown) because both variables come from the input climate data, while the other four main surface energy fluxes including SW_{out}, LW_{out}, H, and LE show significant differences due to MTEB. The differences in energy fluxes can be well explained by the differences in surface properties at all three grid-cells for the different latitudes. For instance, the difference in SW_{out} between MICT-teb and MICT can be explained by the difference in albedo; the difference in LW_{out} can be explained by the difference in T_{surf}; the difference in H (or LE) can be explained by the difference in T_{surf} and / or C_d (surface drag coefficients). This correlation agrees well with theoretical equations (Eqs. (2)-(4)).

The variations in surface properties are related to the modifications made to represent the PFT-specific information in MICT-teb. Regarding albedo, grass leaves generally have a higher albedo (0.15-0.16) than tree leaves (0.10-0.14) (Table S3), while the albedo of bare soil varies, in the model, depending on soil moisture, ranging from ~0.05 in moist areas to ~0.5 in dry areas (Fig. S1). In the tropical grid-cell, all of the four grass PFTs show a higher albedo than the grid-cell mean (0.125), whereas some of the six tree PFTs show a lower albedo than the grid-cell mean and others showing a higher value. The peat PFT has the same leaf albedo value as grass PFTs, but its albedo, as shown in Fig. 3b, is lower than the grid-cell mean, which is due to the higher fraction of bare soil (with a small albedo of 0.093) for this PFT (~70%) relative to the other four grass PFTs (2-30%). We note that the cover fraction of a PFT in the model includes both valid vegetation and bare soil. The albedo of a PFT is calculated as the area-weighted sum of the albedo of its leaves and the albedo of its bare soil. In temperate and boreal regions, the albedo of one PFT is greatly influenced by snow cover fraction owing to the significantly higher albedo of snow (Table S2). Consequently, the pattern of the difference in albedo between MICT-teb and MICT (Figs. 3 (g) and (l)), closely resembles the difference in snow cover fraction (Fig. S4) for temperate and boreal grid-cells. Regarding C_d, the surface drag coefficient, its variations are determined by variations in PFT-specific T_{surf} and H_{rough} (roughness height): the smaller the T_{surf} and the larger the H_{rough}, the larger the C_d. The theoretical relationship can be reproduced well from the comparison of simulated results between MICT-teb and MICT in Fig. 3.

https://doi.org/10.5194/gmd-2023-207
Preprint. Discussion started: 22 November 2023

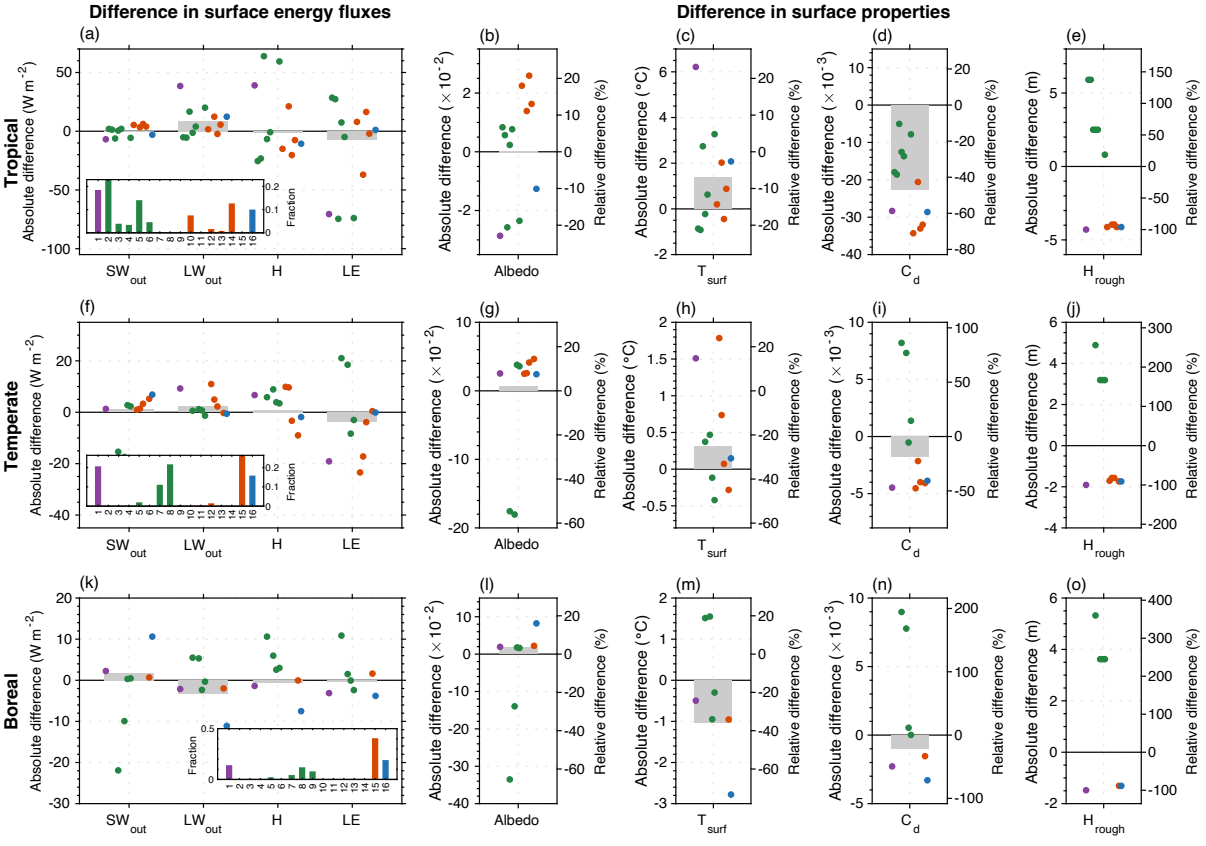

Figure 3: Differences in surface energy fluxes (the first column) and surface properties (from the second to the last column) between MICT-teb and MICT for three grid-cells located at tropical (17°N, 155°W), temperate (51°N, 101°W), and boreal (71°N, 147°E) regions, respectively. The surface energy fluxes include outward shortwave radiation (SW_{out}), outward longwave radiation (LW_{out}), sensible heat flux (H), and latent heat flux (LE). The surface properties include albedo (Albedo), surface temperature (T_{surf}), surface drag coefficient (C_d), and roughness height (H_{rough}). The gray bar in the background indicates the grid-scale difference in each variable. The colored points from left to right indicate the differences between 16 PFTs in MICT-teb and the grid-scale values in MICT, and the missing points indicate the cover fraction of one PFT is zero for the grid-cell. The insets in the first column show the cover fraction of 16 PFTs for the grid-cell. The 16 PFTs are bare soil (PFT1, in purple), trees (PFT 2-9, in green), grass (PFT 10-15, in orange), and peat grass (PFT16, in blue). Please see Table S2 for the long name of 16 PFTs.

When extending to the whole NH, the correspondence between differences in surface heat fluxes and differences in surface properties at grid-cell scale can still be observed (Figs. 4-5 and S5). Additionally, certain latitudinal trends begin to emerge in the difference between MICT-teb and MICT. Based on our modifications to calculate PFT-specific leaf albedo and H_{rough}, the most immediate variations in SW_{out} or turbulent fluxes (H and LE) lead to the final direction of differences in T_{surf} between MICT-teb and MICT for different PFTs (Table 2). For bare soil, whose H_{rough} is set to 0 in MICT-teb, the smaller H and LE result in a higher T_{surf} (up to 3 °C) compared to MICT across almost all areas with bare soil. For tree PFTs, the higher H and LE due to the larger H_{rough} contributes overall to a cooler T_{surf} (-3-0 °C) at low latitudes, while the more important decrease in SW_{out} due to the smaller albedo in MCT-teb results in a warmer T_{surf} (0-2 °C) at high latitudes. With

https://doi.org/10.5194/gmd-2023-207
Preprint. Discussion started: 22 November 2023


Geoscientific Model Development Discussions

the same dominant role of the H_{rough} variation at low latitudes and of the albedo variation at high latitudes, the grass and peat grass show a warmer T_{surf} (0-3 °C) at low latitudes but a cooler T_{surf} (-1-0 °C for grass and -2-0 °C for peat grass) at high latitudes in MICT-teb. As a result, the grid-cell T_{surf} simulated by MICT-teb is 0-2°C higher in most regions in the NH while slightly cooler (-1-0°C) in the north of 60°N and some arid regions than MICT (Fig. 5b).

https://doi.org/10.5194/gmd-2023-207
Preprint. Discussion started: 22 November 2023

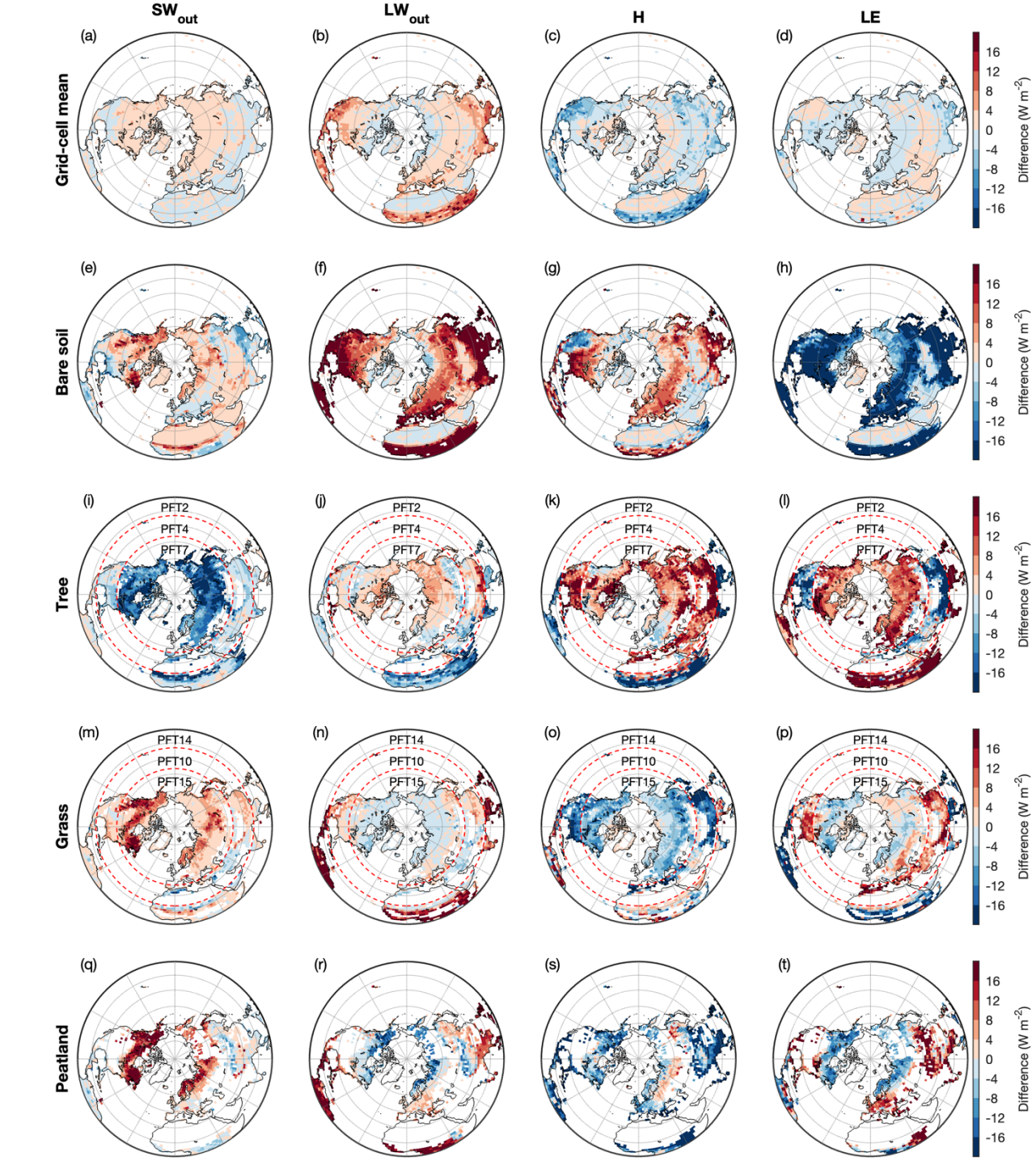

Figure 4: Spatial patterns of differences in surface energy fluxes including outward shortwave radiation (SW_{out}), outward longwave radiation (LW_{out}), sensible heat flux (H), and latent heat flux (LE) between MICT-teb and MICT over the Northern Hemisphere. The first to fifth lines show the difference in each flux between the grid-cell mean, bare soil (PFT1), tree (a

https://doi.org/10.5194/gmd-2023-207
Preprint. Discussion started: 22 November 2023

Geoscientific Model Development Discussions

combination of PFT2 (Tropical broad-leaved evergreen tree) in the south of 20°N, PFT4 (Temperate needleleaf evergreen) between 20°N and 40°N and PFT7 (Boreal needleleaf evergreen tree) in the north of 40°N), grass (a combination of PFT14 (Topical C3 grass) in the south of 20°N, PFT10 (Temperate C3 grass) between 20°N and 40°N, and PFT15 (Boreal C3 grass) in the north of 40°N), and peatland grass (PFT16) from MICT-teb and the grid-cell mean from MICT, respectively. The three PFTs for the tree or grass are combined just in order to show as many results as possible, and only one PFT is shown in each grid-cell.

https://doi.org/10.5194/gmd-2023-207
Preprint. Discussion started: 22 November 2023

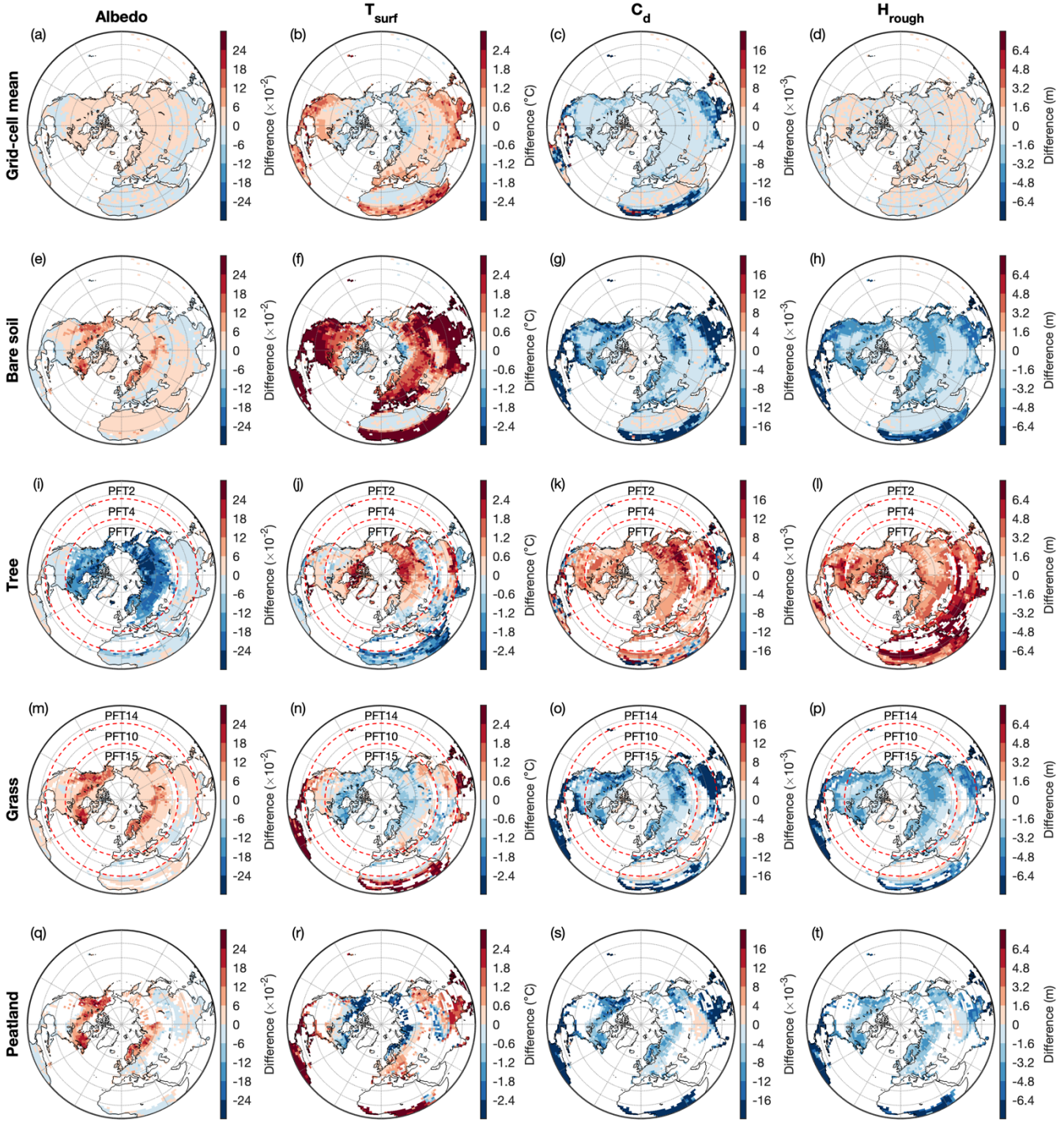

Figure 5: Same as Fig. 4, but for spatial patterns of differences in surface properties including albedo (Albedo), surface temperature (T_{surf}), surface drag coefficients (C_d), and roughness height (H_{rough}) between MICT-teb and MICT over the Northern Hemisphere.

https://doi.org/10.5194/gmd-2023-207
Preprint. Discussion started: 22 November 2023

Geoscientific Model Development Discussions

Table 2. Summary of latitudinal trends of differences in surface properties and associated differences in surface energy fluxes between MICT-teb and MICT. The red and blue arrows indicate the warming and cooling effects on T_{surf}, respectively. The two arrows indicate a stronger effect than one arrow.

PFT type	Regions	ΔAlbedo	ΔSW_{out}	ΔH_{rough}	H and LE	ΔT_{surf}
Bare soil	Low / High-latitudes	…	…	↓	↓↓	
Tree	Low-latitudes	↓	↓	↑	↑↑	
	High-latitudes	↓	↓↓	↑	↑	
Grass	Low-latitudes	↑	↑	↓	↓↓	
	High-latitudes	↑	↑↑	↓	↓	
Peat grass	Low-latitudes	↑	↑	↓	↓↓	
	High-latitudes	↑	↑↑	↓	↓	

https://doi.org/10.5194/gmd-2023-207
Preprint. Discussion started: 22 November 2023

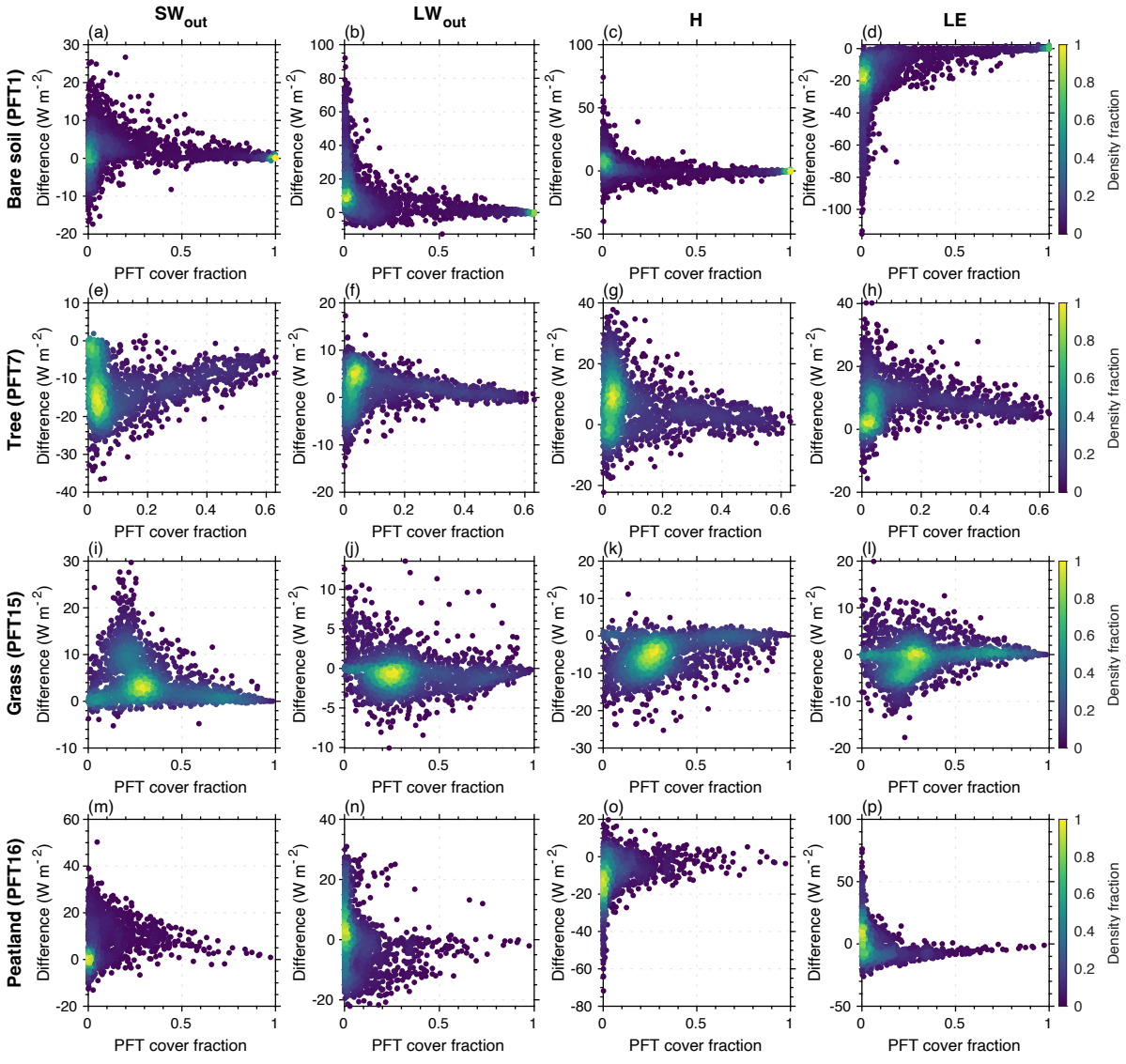

Figure 6: Scatter plot of differences in surface energy fluxes between MICT-teb and MICT versus vegetation cover fraction for bare soil (PFT1), tree (PFT7), grass (PFT15), and peatland grass (PFT16). The surface energy fluxes include outward shortwave radiation (SW_{out}), outward longwave radiation (LW_{out}), sensible heat flux (H), and latent heat flux (LE). The color of each point represents the density fraction of grid-cells.

Another interesting result is the relationship between differences in surface heat fluxes or properties between MICT-teb and MICT and the vegetation cover fraction. As mentioned in Sect. 3.1, the difference between the two versions should become smaller where one PFT's tends to become more dominant in the grid-cell. When the cover fraction of one PFT approaches 100%, there will be no difference between the grid-cell mean and the specific PFT. Taking four PFTs as examples, we found this pattern both for surface heat fluxes (Fig. 6) and surface property variables (Fig. S6).

https://doi.org/10.5194/gmd-2023-207
Preprint. Discussion started: 22 November 2023

Geoscientific Model Development
Discussions
Open Access
EGU

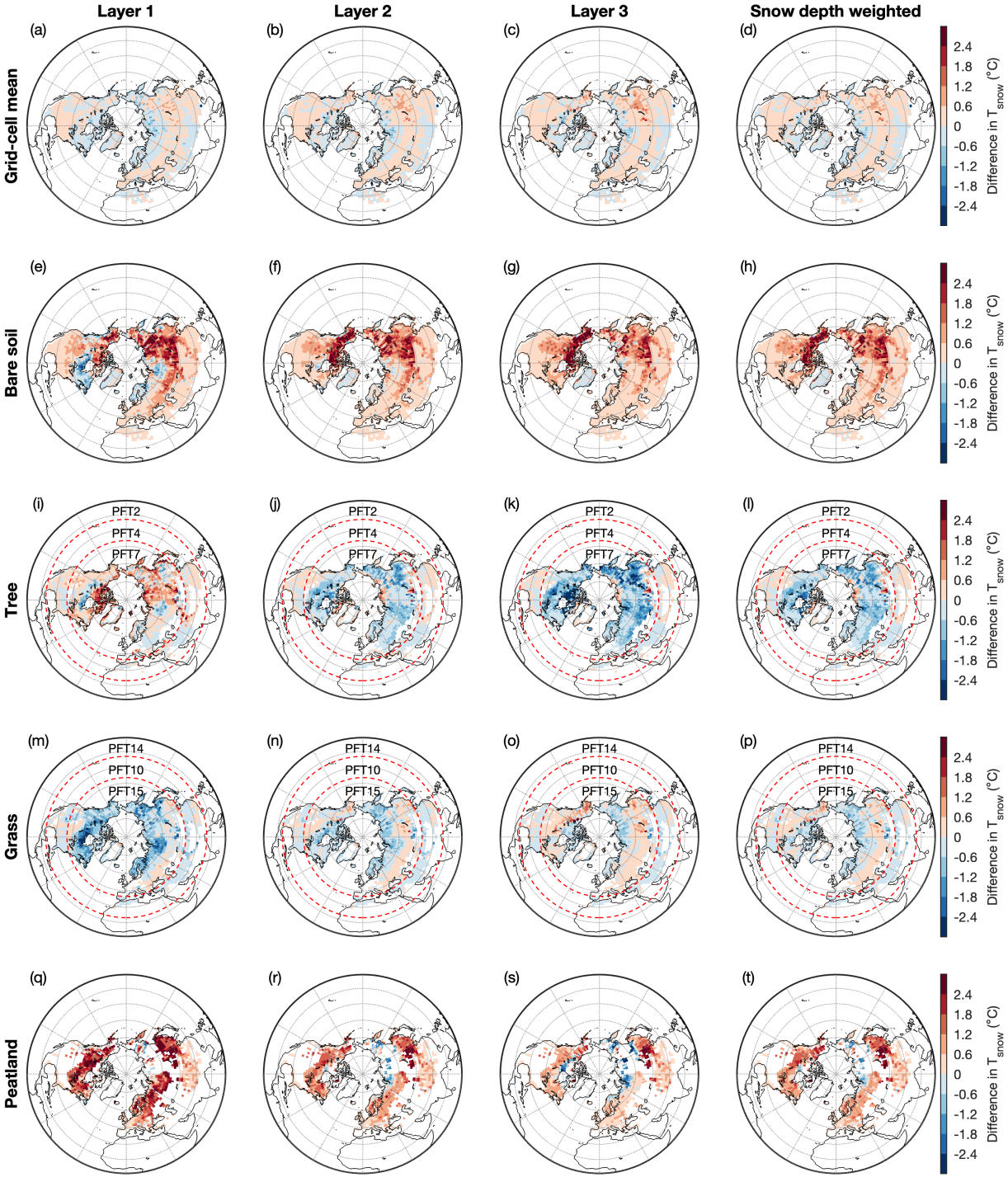

https://doi.org/10.5194/gmd-2023-207
Preprint. Discussion started: 22 November 2023

Geoscientific Model Development Discussions

Figure 7: Spatial patterns of difference in T_{snow} between MICT-teb and MICT for three snow layers and the snow depth weighted results over the Northern Hemisphere. The snow layers from up to down are numbered 1-3, respectively. The snow depth weighted results are shown due to the different snow layer depth across different grid-cells.

5.1.2 Snow energy budgets

Figure 7 presents differences in T_{snow} (ΔT_{snow}) of three snow layers between MICT-teb and MICT for the grid-cell mean and four PFT types. Overall, the grid-cell ΔT_{snow} follows the ΔT_{surf} between the two versions, with an up to 1 °C warmer snow layer across most areas in MICT-teb. The correlation of ΔT_{snow} and ΔT_{surf} weakens from the uppermost snow layer ($T_{snow,1}$) to the bottom one ($T_{snow,3}$), especially for tree and grass PFTs (Table S5). For the two PFTs, the differences in the two thermal parameters (c_{snow} and λ_{snow}) play a more important role than ΔT_{surf} in shaping the spatial pattern of ΔT_{snow} in the bottom two layers (Table S5 and Figs. S7 and S8). Since the snow depth for each layer is not fixed like soil layers (Fig. 1), we calculate the snow-depth weighted ΔT_{snow} between the two versions (the last column in Fig. 7). The differences in c_{snow} and λ_{snow} are more important in determining the spatial patterns of the snow-depth weighted ΔT_{snow}.

5.1.3 Soil energy budgets

Figure 8 presents the differences in T_{soil} (ΔT_{soil}) of four soil layers between MICT-teb and MICT for the grid-cell mean and four PFT types. Similar to the ΔT_{snow}, the ΔT_{soil} shows a larger and significantly positive correlation ($R = 0.31\text{-}1.00$, $p < 0.05$) with differences in the starting point of heat conduction (T_{surf} for 0°-30°N and $T_{snow,3}$ for 30°N-90°N) than the two thermal parameters of soil (Table S6). The grid-cell mean T_{soil} for the four soil layers simulated by MICT-teb is ~0.6 °C warmer than MICT in the north of 30°N while ~1.2 °C warmer in the tropics across four soil layers. The PFT-specific ΔT_{soil} show considerably different magnitudes and directions across four PFT types: the T_{soil} for bare soil is ~3 °C higher in MICT-teb than MICT; the T_{soil} for tree and peat grass is 0.6-3 °C lower; and the T_{soil} for grass is 0.6-3 °C higher. Despite using the same parameter values of leaf albedo and H_{rough} between peat grass and C3 grass, the T_{soil} of peat grass is 0.6-3 °C lower at high latitudes in MICT-teb, which could be related to the considerably different spatial patterns of the two soil thermal parameters between peat grass and C3 grass (Table S6 and Figs. S9 and S10).

As mentioned in Sect. 3.3, the liquid SM (SM_{liquid}), frozen SM (SM_{frozen}), and SOC are three key factors influencing the two thermal parameters of soil (Eqs. (6) and (7)). Despite the previous soil-tile-based hydrologic processes and PFT-based carbon cycle in MICT, the soil thermal parameters (c and λ) are calculated with the grid-cell mean values of SM_{liquid}, SM_{frozen}, and SOC in that version. With far wetter SM (≥200%, Figs. S11 and S12) and far more SOC storage (≥200%, Fig. S13), the peat PFT has a ~200% higher c (Fig. S9) and a ~100% higher λ (Fig. S10) than grid-cell mean. Such large Δc and $\Delta\lambda$ compared to grass (40% higher / lower c and 20% higher / lower λ than grid-cell mean) leads to a lower T_{soil} for peat

https://doi.org/10.5194/gmd-2023-207
Preprint. Discussion started: 22 November 2023


Geoscientific Model Development Discussions

grass in MICT-teb than in MICT (Fig. 8). Besides the peat grass PFT, the important role of the three factors in regulating T_{soil} can also be found for other PFTs. For example, we found ~100% less SOC storage in bare soil than the grid-cell mean, which contributes to the higher T_{soil} for bare soil due to the absence of SOC's insulating impacts.

405

https://doi.org/10.5194/gmd-2023-207
Preprint. Discussion started: 22 November 2023

Geoscientific Model Development
Discussions
Open Access
EGU

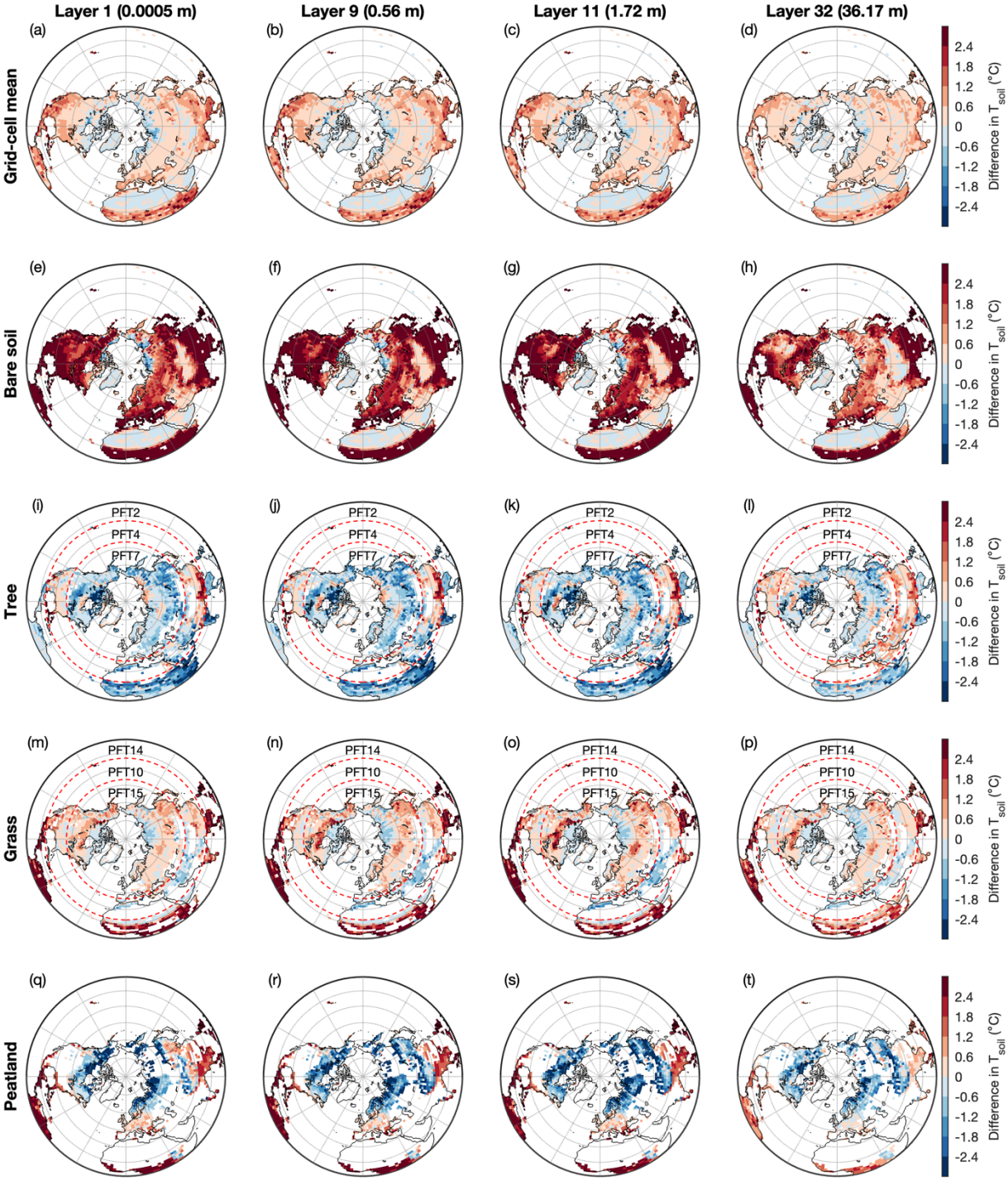

Figure 8: Same as Fig. 7, but for spatial patterns of differences in T_{soil} between MICT-teb and MICT for four soil layers over the Northern Hemisphere.

https://doi.org/10.5194/gmd-2023-207
Preprint. Discussion started: 22 November 2023


Geoscientific Model Development Discussions

5.2 Long-term impacts on energy, hydrology, and carbon cycle

5.2.1 Energy

Regarding the long-term impacts of representing the sub-grid energy budgets in the model, we compare the simulated results among S0, S1, and S2 for three aspects: energy budgets, hydrology, and carbon cycle (Figs. 9-11). For the energy budgets, we found that the difference in T_{surf} between S1 and S0, or between S2 and S0 appears in the first two to three years and then remains stable throughout all three simulation periods (Fig. 9a). By the end of period C, the ΔT_{surf} over the NH between S2 and S0 remains at 0.37 °C (+3.5%). A very similar ΔT_{surf} (0.38 °C, 3.6%) can be observed between S1 and S0, suggesting that the surface energy budgets can quickly respond to variations in surface properties including albedo and roughness. As the heat moves down, the determining role of T_{surf} in influencing the heat conduction in soil (Table S6) makes the T_{soil} at the 1st (0.0005 m), 11st (1.72 m), and 32nd (36.17 m) layers over the NH warmer by 0.44 °C (3.3%), 0.45 °C (3.5%) and 0.51 °C (3.6%) respectively, by the end of period C under S2 than that under S0. But it takes a longer time to reach stability for T_{soil} at the bottom soil layers than the upper ones (Fig. 9 (c), (e), and (g)). The SOC, acting as an insulator, could regulate the soil thermics, especially in summer (Zhu et al., 2019). Nevertheless, the difference in mean annual or monthly T_{soil} at all soil layers between S1 and S2 is very small, no more than 0.18 °C (1.2%). Therefore, the long-term effects of MTEB on surface or soil energy budgets is subtle in the simulations of this study.

https://doi.org/10.5194/gmd-2023-207
Preprint. Discussion started: 22 November 2023

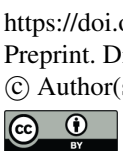

Geoscientific Model Development Discussions

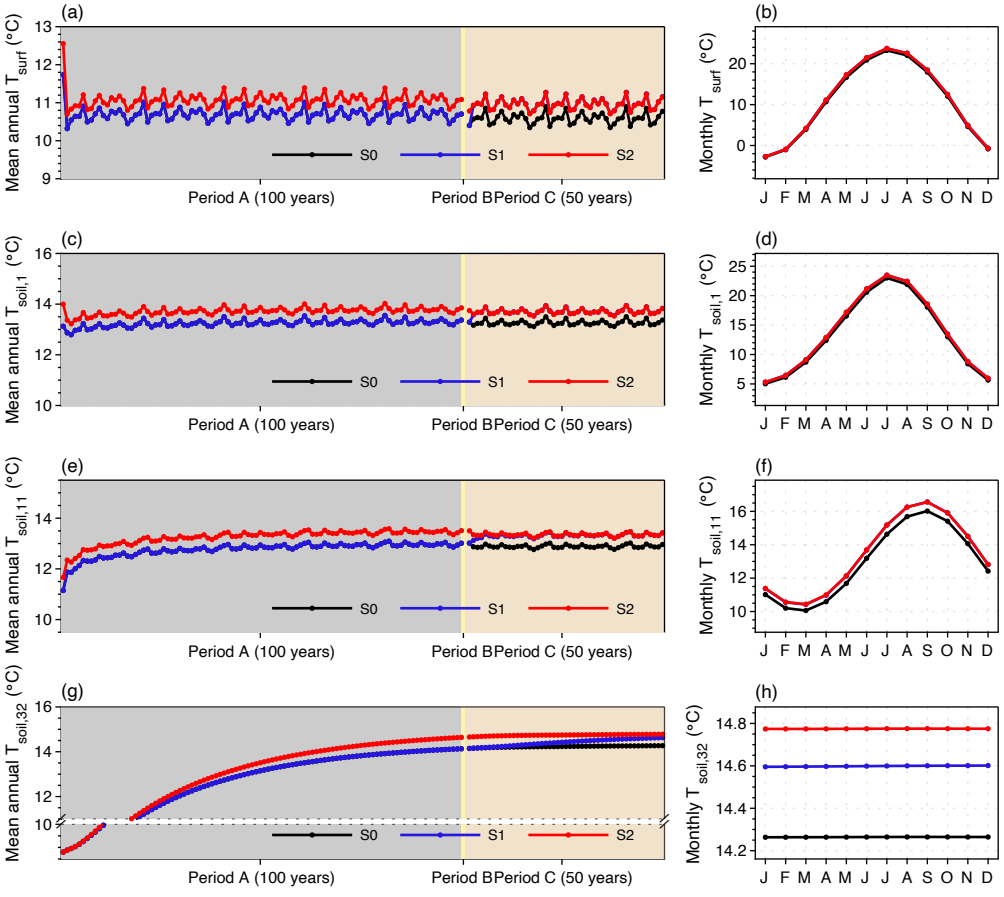

Figure 9: Time series and seasonal cycle of surface temperature (T_{surf}) and soil temperature for three soil layers ($T_{soil,1}$, $T_{soil,11}$, and $T_{soil,32}$) over the Northern Hemisphere from three simulations. The annual values are calculated using the yearly average, and the monthly values are calculated using the average of the last ten years in period C.

5.2.2 Hydrology

The hydrology processes can respond to the representation of sub-grid energy budgets as quickly as temperature, taking up to five years to reach the stability for both surface water fluxes including evapotranspiration (ET) and surface runoff (Q), as well as subsurface water fluxes such as drainage (D) (Fig. 10). Overall, MICT-teb shows a smaller ET (-8.7 mm yr^{-1}, -2.3%), but a larger D (+11.8 mm yr^{-1}, 8.3%) over the NH compared to MICT. When separating sub-components of ET and soil tiles, we found that the decreased ET is mainly contributed by the decreased E_{trans} (transpiration) from tree PFTs and the decreased E_{subli} (sublimation) from the grass PFTs, with values of -3.7 mm yr^{-1} and -3.0 mm yr^{-1} per grid-cell over the NH, respectively (Fig. S14). Spatially, the decreased E_{trans} for tree PFTs are mainly distributed in tropical regions and eastern North America while the decreased grass E_{subli} is located at high latitudes (Fig. S15). Both of these decreases are related to the variations in

https://doi.org/10.5194/gmd-2023-207
Preprint. Discussion started: 22 November 2023

Geoscientific Model Development Discussions

surface properties (the decreased C_d and / or decreased T_{surf}) in MICT-teb (Fig. 5). As a result of the balance between the variations of ET and runoff, the SM (0-2 m) in MICT-teb is 9.9 kg m^{-2} (1.8%) wetter than in MICT (Fig. 10).

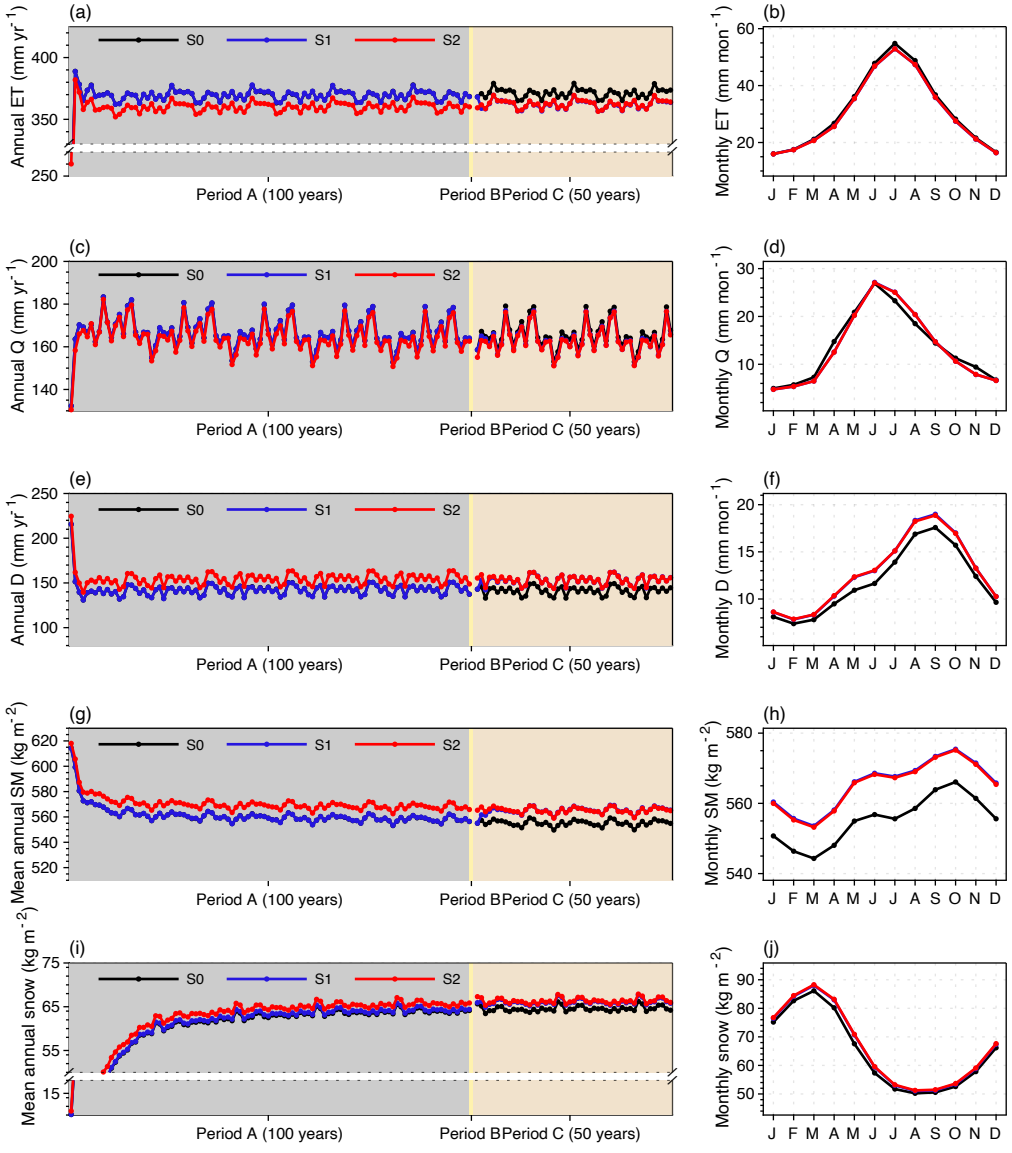

445 **Figure 10: Time series and seasonal cycle of hydrology variables including evapotranspiration (ET), surface runoff (Q), drainage (D), soil moisture (SM), and snow over the Northern Hemisphere from three simulations.**

https://doi.org/10.5194/gmd-2023-207
Preprint. Discussion started: 22 November 2023


Geoscientific Model Development Discussions

5.2.3 Carbon

In response to the warmer and wetter soils (Fig. S16), vegetation productivity is significantly enhanced over the NH in MICT-teb, with a 1.9 PgC yr^{-1} (2.7%) larger GPP and a 0.8 PgC yr^{-1} (2.7%) larger NPP under S2 than S0 (Fig. 11). The enhanced productivity is primarily driven by tree PFTs across almost all NH regions and grass PFTs at mid- and low latitudes, while the productivity of peatland grass is somewhat lower due to the cooler soil (Figs. S16 and S17). The warmer soil also accelerates the heterotrophic respiration rate (R_h) for tree and grass PFTs, along with the variation in SM. Compared to S0, S2 has a larger SOC (+58.5 PgC, 9.0%) for tree PFTs but almost unchanged SOC storage (22.5 PgC, 2.8%) for grass PFTs. Despite being the smallest SOC pool (~27%, ~600 pg C) (Hugelius et al., 2014, 2016, 2020; Lindgren et al., 2018) among the three vegetated soil tiles as a result of the small peatland area (~3% of vegetated land in the NH), the peatland PFT's SOC storage increases by 85.8 PgC, accounting for more than a half of the total SOC increase from S0 to S2 (Fig. 12). The cooler soil throughout the entire vertical profile of peat PFT promotes the SOC accumulation by significantly slowing down the soil respiration ($R = 0.38$, $p < 0.01$), showing a more critical role in regulating the SOC decomposition than SM ($R = 0.20$, $p < 0.01$). Moreover, unlike the energy and water processes, the difference in SOC (ΔSOC) between S2 and S0 is obviously larger than that between S1 and S0 (~7 PgC), and from a temporal perspective, it exists after period B and then keeps stable until the end of period C (Fig. 11(g)). This means that the ~170 PgC ΔSOC between S2 and S0 has been accumulated since the peat initiation and the long-term effects of MTEB on soil carbon cannot be neglected.

https://doi.org/10.5194/gmd-2023-207
Preprint. Discussion started: 22 November 2023

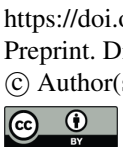

Geoscientific Model Development Discussions

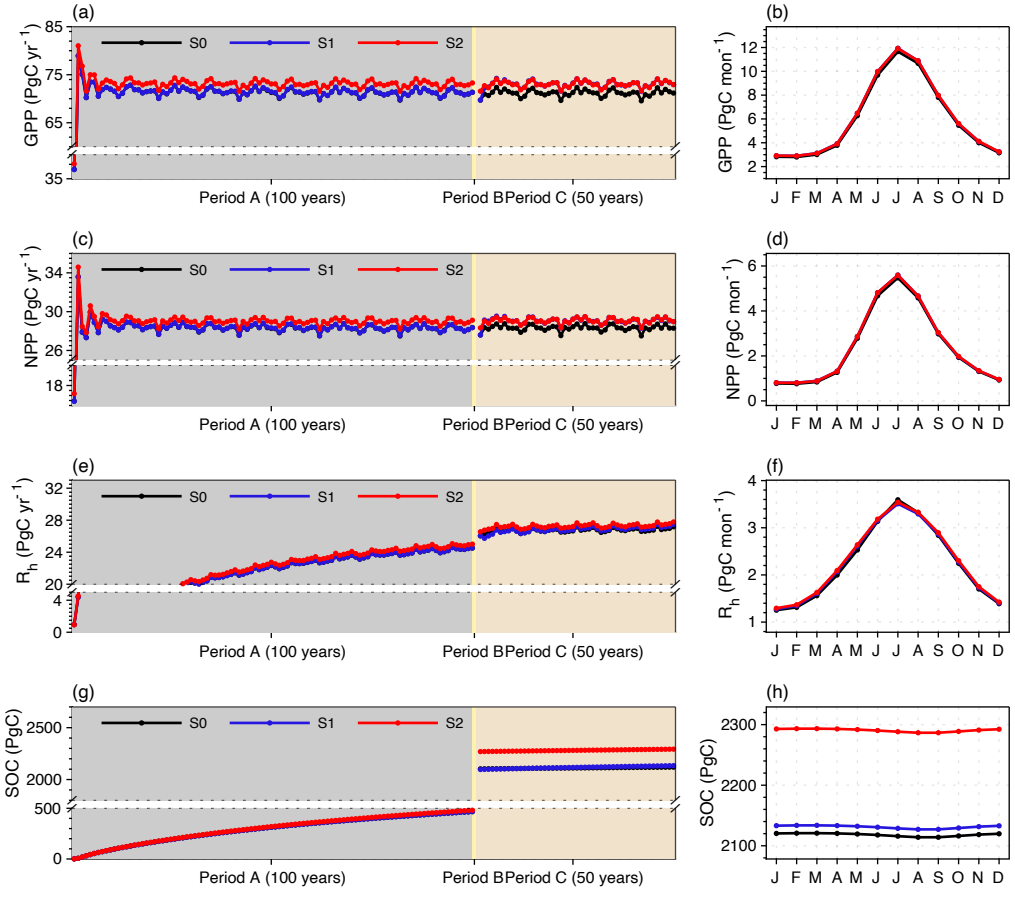

465

Figure 11. Time series and seasonal cycle of carbon-related variables including gross primary productivity (GPP), net primary productivity (NPP), heterotrophic respiration (R_h), and soil organic carbon (SOC) over the Northern Hemisphere from three simulations. The depth for R_h and SOC is 0-38 m.

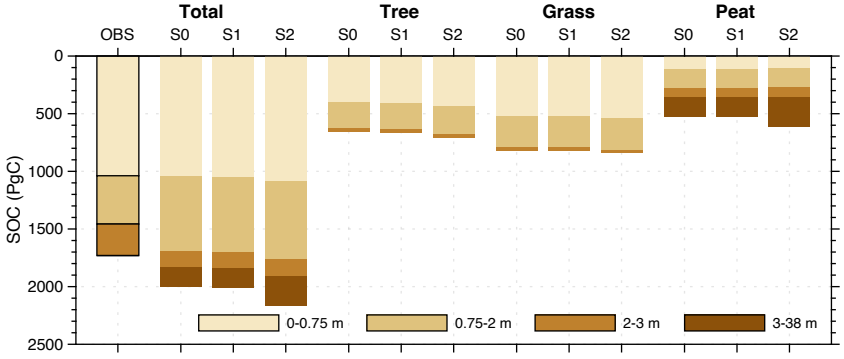

470

Figure 12. Vertical composition of soil organic carbon (SOC) for all PFTs and three vegetated soil tiles (tree, grass, and peat) over the Northern Hemisphere from an observation-based SOC map and three simulations. For observed data, we only show the results

https://doi.org/10.5194/gmd-2023-207
Preprint. Discussion started: 22 November 2023

Geoscientific Model Development Discussions

for all PFTs due to the lack of biome information. For simulations, all values are calculated using the average of the last ten years in period C.

6 Evaluation and potential application

6.1 Evaluation of the simulated temperature

To evaluate the energy processes in the new version, we first compare the simulated T_{surf} with satellite-derived land surface temperature (LST) from MODIS (the Moderate Resolution Imaging Spectroradiometer) (Wan, 2013, 2014) (Fig. 13). The MODIS LST product employed in this study (MOD11C3 Version 6, available at https://lpdaac.usgs.gov/products/mod11c3v006/) records the radiative skin temperature of the land surface at a spatial resolution of 0.05° × 0.05°, providing monthly daytime and nighttime values spanning from 2000 to the present. To keep consistency with the period covered by the MODIS data, we extend our simulations (S0 and S2) to the year 2020 using the transient climate data from CRU-JRA v2.3, atmospheric CO_2 concentration, and annual land cover maps from TRENDY project. Compared to the MODIS product, MICT and MICT-teb can reproduce the spatial pattern of mean annual satellite-derived LST for 2001-2020 (Figs. 13(a)-(c)), but with an overestimation of up to 3 °C in wet regions such as tropical regions, Europe, and eastern North America, as well as an underestimation of up to 3 °C in dry areas and northeastern Asia (Figs. 13(d) and (e)). Including the representation of PFT-specific energy budgets slightly alleviates the underestimation of LST by MICT in western North America and the overestimation in northern Europe and western Siberia, but aggravates the overestimation in tropical regions and eastern North America (Fig. 13(f)). On the one hand, 1) the under-representation of some important processes in the model such as the parameterization of ET and snow insulation and the uncertainties of climate forcing data (Guimberteau et al., 2018; Peng et al., 2016; Domine et al., 2016), 2) the missing data across dry areas and cloudy-weather days in the MODIS product (± 2 °C bias compared to ground-truth data) (Li et al., 2014; Wan, 2014; Westermann et al., 2012), and 3) the considerable disagreements in land cover maps (Fig. S18) and spatial resolutions (2° versus 0.05°) between simulations and the MODIS product could result in the difference in T_{surf} between simulations and MODIS. On the other hand, the consistent spatial distributions of the difference in T_{surf} implies the systematic biases / gaps could have existed between the model and the satellite product. Since the radiative skin temperature reported by MODIS are used to measure canopy temperature, the significant difference in canopy and surface temperature, especially in forest ecosystems could contribute to the difference in T_{surf} in Fig. 13, e.g. the ~3 °C difference between the ground temperature and the MODIS LST found in Amazon evergreen forests (Gomis-Cebolla et al., 2018).

https://doi.org/10.5194/gmd-2023-207
Preprint. Discussion started: 22 November 2023

Geoscientific Model Development Discussions

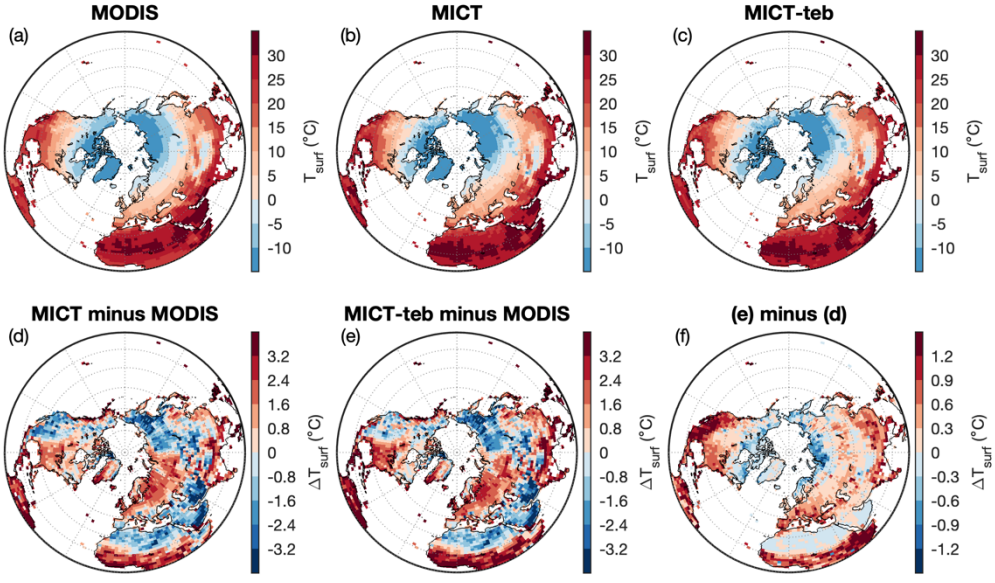

Figure 13. Evaluation of simulated surface temperature (T_{surf}) with land surface temperature (LST) from MODIS. (a)-(c), Spatial pattern of mean annual LST for 2001-2020 from MODIS, MICT, and MICT-teb. (d) and (e), Spatial pattern of the difference in mean annual T_{surf} for 2001-2020 between MICT (d) or MICT-teb (e) and MODIS. (f), Spatial pattern of the difference in (e) and (d).

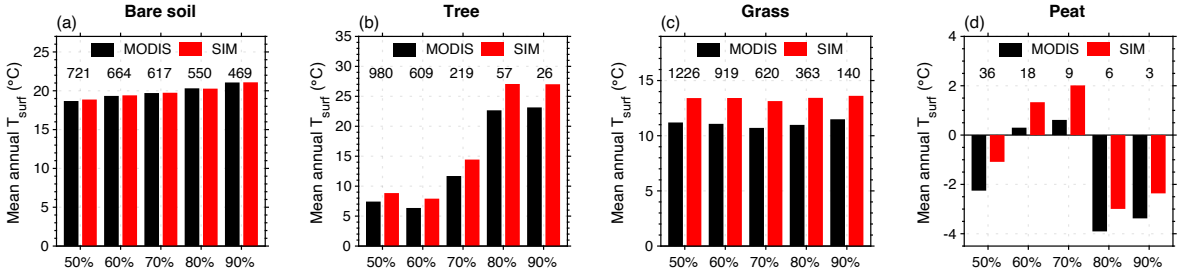

Figure 14. Evaluation of simulated surface temperature (T_{surf}) with land surface temperature (LST) from MODIS by PFT type. (a)-(d), Mean annual T_{surf} for four PFT types (bare soil, tree, grass, and peat) for 2001-2020. The grid-cells for each PFT type are selected with five threshold fractions (50%, 60%, 70%, 80%, 90%). The numbers of grid-cells for each group of bars are shown.

In light of the new feature of MICT-teb to simulate PFT-specific energy budgets, we compare the simulated and satellite-based T_{surf} over grid-cells dominated by four PFT types: bare soil, tree, grass, and peatland from simulations (Fig. 14). Despite the systematic biases in the simulations, the model can produce a comparable T_{surf} to MODIS for four PFT types. Also, the model can capture the variations of LST from MODIS well when altering the threshold fractions for grid-cell selection from 50% to 90%. For tree, grass, and peat, due to their extensive coverage in wet areas, the simulated T_{surf} is 1-3 °C warmer than grid-cell LST from MODIS for all threshold fractions. For bare soil, the underestimation of T_{surf} in desert

https://doi.org/10.5194/gmd-2023-207
Preprint. Discussion started: 22 November 2023

Geoscientific Model Development Discussions

areas is offset by the overestimation in Greenland (Figs. 13(d) and (e)). The notable biases when using a 90% threshold fraction, a near-complete coverage of one PFT type within one grid-cell, suggests the disagreement between the model and satellite products should be attributed to the gap between MODIS and the original version, rather than the separation of PFT-specific energy budgets.

For the simulated soil temperature, we evaluate the T_{soil} at 20 cm with in-situ observations across 268 sites from Russian Meteorological Stations (Sherstiukov, 2012). The time period of the site data spans from 1980 to 2000. To avoid the bias resulting from missing values, we exclude 69 sites containing missing values for a specific month in over half of years, either from the observed data or simulations. As shown in Fig. 15 and Fig. S19, the simulated mean annual T_{soil} at 20 cm from MICT and MICT-teb can well reproduce the spatial gradient of observed values, with a strong and positive correlation ($R = 0.94$; $p < 0.001$). However, when it comes to the mean seasonal cycle of T_{soil}, a warmer T_{soil} during winter but a cooler T_{soil} during summer are simulated in comparison with observations, especially for sites located in continuous permafrost regions (Fig. 15(c)). Apart from climate forcing data uncertainties as suggested by Guimberteau et al. (2018), SM, SOC, and snow cover are three factors most likely to regulate the seasonal amplitude of T_{soil}. Guimberteau et al. (2018) has demonstrated that the snow insulation is underestimated by MICT when using both GSWP3 or CRUNCEP datasets to force the model. This implies that, from a snow perspective, our simulation should exhibit an amplified seasonal cycle. Conversely, the simulated dampened seasonal amplitude of T_{soil} indicates the potentially crucial roles of SM and SOC. Due to the inclusion of peat PFT in our simulations and the use of simulated SOC rather than prescribed SOC maps to regulate soil thermal properties, the uncertainties in prescribed peatland maps and simulated SOC could propagate the uncertainties in T_{soil}. Moreover, we extract LST in 2000 across these sites from MODIS data (Fig. S20) and find a weak correlation between the bias in T_{surf} against MODIS and the bias in T_{soil} against site data ($R = 0.19$, $p < 0.01$ for all sites; $R = -0.01$, $p > 0.05$ for continuous permafrost sites; $R = 0.03$, $p > 0.05$ for other sites), suggesting the potential uncertainties in observed data from different sources.

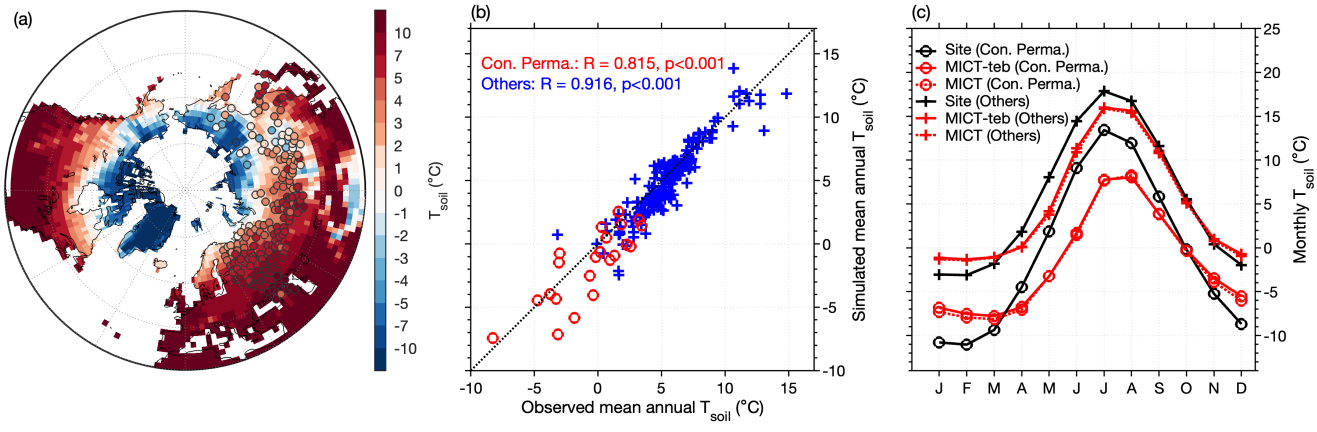

https://doi.org/10.5194/gmd-2023-207
Preprint. Discussion started: 22 November 2023

Geoscientific Model Development Discussions

Figure 15. Evaluation of simulated soil temperature (T_{soil}) at 20 cm with site observations. (a), Spatial patterns of mean annual T_{soil} at 20 cm during the period 1980-2000 from the simulation of MICT-teb, with the values of 199 sites shown as color filled circles. (b), Simulated (from MICT-teb) versus observed mean annual T_{soil} at 20 cm across all sites. (c), Mean seasonal cycle of site-averaged T_{soil} at 20 cm from site observations, MICT-teb, and MICT. The sites in (b) and (c) are divided into those located in continuous permafrost (Con. Perma.) regions (22 sites, circle markers) and others (177 sites, markers of plus sign) according to the permafrost map of Brown (2002).

As for the impacts of multi-tiling energy budgets on T_{surf}, our simulations suggest that the variation in albedo plays a dominant role at high latitudes, whereas the variation in H_{rough} is more significant at low latitudes (Table 2). This result is consistent with numerous studies on the biophysical feedbacks of land cover change, as the use of PFT-specific H_{rough} and albedo for tree PFTs can be seen as an analogy to reforestation or afforestation, while the use of PFT-specific H_{rough} and albedo for grass PFTs parallels the case of deforestation or forest degradation. Flux tower measurements, satellites, and climate models have revealed that tropical tree planting mitigates warming through evaporative cooling while the low albedo of new boreal forests is a positive climate forcing (Betts, 2000; Bonan, 2008; Peng et al., 2014; Su et al., 2023). In contrast, the conversion of forests to grasslands ,or forest degradation show a warming effect in tropical regions but a cooling effect in boreal regions (Lawrence and Vandecar, 2015; Ramdane Alkama and Alessandro Cescatti, 2016; Li et al., 2022; Zhu et al., 2023). This consistency confirms the modifications we made in the new MICT version.

6.2 Improvements for permafrost simulations

Given the crucial role of T_{soil} in permafrost simulations, we compare the simulated permafrost extent from MICT and MICT-teb with two independent permafrost datasets from Brown et al. (2002) and Obu et al. (2019), hereafter named Brown2002 and Obu2019, respectively (Fig. 16). Brown's map is compiled based on national / regional maps and empirical knowledge, categorizing permafrost into four classes: continuous permafrost (permafrost fraction > 0.9), discontinuous permafrost (0.5 ~ 0.9), sporadic permafrost (0.1 ~ 0.5), and isolated patches (0 ~ 0.1) (Brown, 2002). Obu's map is generated by using a temperature model to simulate soil thermal regimes in 3D at 300 m × 300 m spatial resolution (Obu et al., 2019). The Obu2019 data provides the absolute fraction of the landscape affected by permafrost when aggregated to a coarser grid-cell (Obu et al., 2019). The simulated permafrost areas are identified following Guimberteau et al. (2018) with two definitions: 1) active layer thickness (ALT) less than 3 m; or 2) T_{soil} of any soil layer remains below 0 °C for at least two years. Since the simulated permafrost areas are very similar between the two definitions, we only show the results using the ALT definition in the manuscript while the results using the T_{soil} definition in supplementary (Fig. S21).

Overall, our models can capture the spatial pattern of continuous permafrost from the two independent datasets. However, the simulated total area of continuous permafrost from MICT, after excluding Greenland (18.5 Mkm^2) is 7.6 and 6.9 Mkm^2 larger than that from Brown2002 and Obu2019, primarily due to the overestimation of continuous permafrost in mid-high latitudes of Asia and the Tibetan Plateau. Given that the grid-cell mean T_{soil} in MICT-teb is ~ 0.5 °C warmer over the NH

https://doi.org/10.5194/gmd-2023-207
Preprint. Discussion started: 22 November 2023

Geoscientific Model Development Discussions

than in MICT (Fig. 8), the total area of continuous permafrost simulated by MICT-teb (15.2 Mkm^2) reduces by 3.3 Mkm^2 than that in MICT. Limited by the grid-cell averaged energy budgets, MICT can't simulate non-continuous permafrost, that is a grid-cell in MICT is either a 100% permafrost or a 100% non-permafrost. While in MICT-teb, the separation of PFT-specific T_{soil} allows the existence of non-continuous permafrost (Fig. 16 (e)). The sum of all four permafrost areas (including three discontinuous classes) in MICT-teb is 18.3 Mkm^2 (continuous 15.2 Mkm^2, non-continuous 3.1 Mkm^2), which is comparable to 16.9 Mkm^2 in Obu2019 (continuous 11.6 Mkm^2, non-continuous 5.3 Mkm^2).

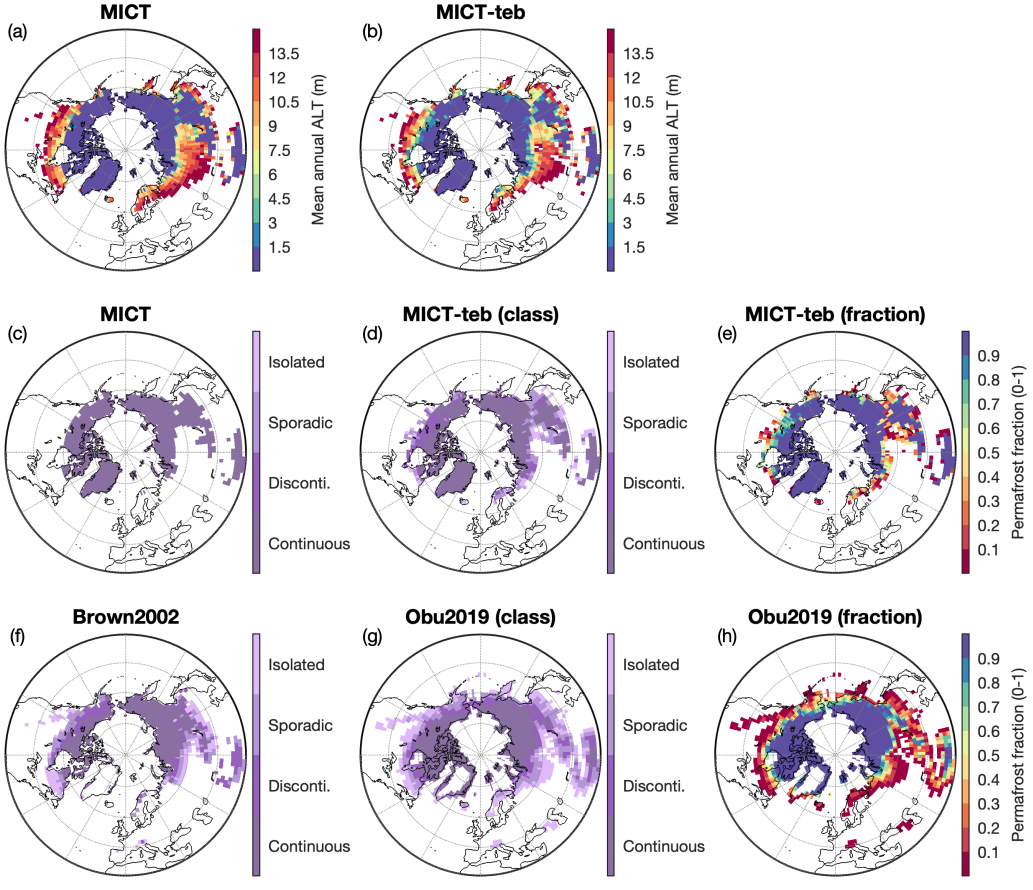

Figure 16. Evaluation of simulated permafrost areas with independent permafrost datasets. (a)-(b), Spatial patterns of active layer thickness (ALT) simulated by MICT and MICT-teb. (c)-(e), Spatial patterns of permafrost areas simulated by MICT and MICT-teb according to the definition of ALT. (f)-(h), Spatial patterns of permafrost areas from Brown2002, Obu2019. The permafrost areas in Figs. (c), (d), (f), and (g) are shown following four permafrost classes from Brown2002, while the permafrost areas in Figs. (e) and (h) are shown with absolute fraction.

https://doi.org/10.5194/gmd-2023-207
Preprint. Discussion started: 22 November 2023

7 Conclusion

This study describes the new representation of multi-tiling energy budgets in the ORCHIDEE-MICT land surface model and investigates its short and long-term impacts on energy, hydrology, and carbon processes. Instead of using grid-cell mean surface properties like roughness height and albedo, the PFT-specific values are employed for each vegetation type and all of the associated energy, hydrology, and carbon processes are modified in the model. Compared to the original version, the separation of PFT-specific energy budgets results in warmer surface and soil temperatures, higher soil moisture, and increased soil organic carbon storage across the Northern Hemisphere. Evaluation with satellite products and site measurements suggests that the new version can reproduce the spatial distributions and seasonal patterns of surface and soil temperature. However, notable positive or negative biases are observed at some regions due to remaining weaknesses of the original ORCHIDEE-MICT model, such as the uncertainties in simulating soil moisture and soil organic carbon, as well as uncertainties in the prescribed peatland map. A notable advancement in the new version is the improved simulation of permafrost extent by accounting for the presence of discontinuous permafrost, which will facilitate various permafrost-related studies based on the model in the future.

Code availability. The ORCHIDEE-MICT-teb model (r8205) code used in this study is open-source and distributed under the CeCILL (CEA CNRS INRIA Logiciel Libre) license. It is deposited at https://forge.ipsl.jussieu.fr/orchidee/wiki/GroupActivities/CodeAvalaibilityPublication/ORCHIDEE-MICT-teb and archived at https://doi.org/10.14768/0954a0e9-6a7a-4006-803e-4db36ef2db88, with guidance to install and run the model at https://forge.ipsl.jussieu.fr/orchidee/wiki/Documentation/UserGuide. Codes to process data, generate all results, and produce all figures are archived at https://doi.org/10.5281/zenodo.10014533 (Xi, 2023).

Author contributions. PC conceived the project. YX implemented multi-tiling energy budgets into ORCHIDEE-MICT. CQ, YZ, DZ, and SP provided general scientific guidance to improve the research and interprete results. YX performed the simulations, did the analysis, and wrote the paper. All authors contributed to commenting and writing on the draft manuscript.

Competing interests. The contact author has declared that none of the authors has any competing interests.

Acknowledgements. This research was supported by the European Union's Horizon 2020 research and innovation programmes under grant agreement No 101003687 (PROVIDE). PC acknowledges support from the CALIPSO (Carbon Loss in Plant Soils and Oceans) project, funded through the generosity of Eric and Wendy Schmidt by recommendation of the Schmidt Futures program. DZ acknowledges support from National Natural Science Foundation of China (No. 42101090).

https://doi.org/10.5194/gmd-2023-207
Preprint. Discussion started: 22 November 2023

References

Best, M. J., Beljaars, A., Polcher, J., and Viterbo, P.: A Proposed Structure for Coupling Tiled Surfaces with the Planetary Boundary Layer, J. Hydrometeorol., 5, 1271–1278, https://doi.org/10.1175/JHM-382.1, 2004.

Betts, R. A.: Offset of the potential carbon sink from boreal forestation by decreases in surface albedo, Nature, 408, 187–190, https://doi.org/10.1038/35041545, 2000.

Bonan, G. B.: Forests and Climate Change: Forcings, Feedbacks, and the Climate Benefits of Forests, Science, 320, 1444–1449, https://doi.org/10.1126/science.1155121, 2008.

Boone, A., Samuelsson, P., Gollvik, S., Napoly, A., Jarlan, L., Brun, E., and Decharme, B.: The interactions between soil–biosphere–atmosphere land surface model with a multi-energy balance (ISBA-MEB) option in SURFEXv8 – Part 1: Model description, Geosci. Model Dev., 10, 843–872, https://doi.org/10.5194/gmd-10-843-2017, 2017.

Boucher, O., Servonnat, J., Albright, A. L., Aumont, O., Balkanski, Y., Bastrikov, V., Bekki, S., Bonnet, R., Bony, S., Bopp, L., Braconnot, P., Brockmann, P., Cadule, P., Caubel, A., Cheruy, F., Codron, F., Cozic, A., Cugnet, D., D'Andrea, F., Davini, P., de Lavergne, C., Denvil, S., Deshayes, J., Devilliers, M., Ducharne, A., Dufresne, J.-L., Dupont, E., Éthé, C., Fairhead, L., Falletti, L., Flavoni, S., Foujols, M.-A., Gardoll, S., Gastineau, G., Ghattas, J., Grandpeix, J.-Y., Guenet, B., Guez, L., Guilyardi, E., Guimberteau, M., Hauglustaine, D., Hourdin, F., Idelkadi, A., Joussaume, S., Kageyama, M., Khodri, M., Krinner, G., Lebas, N., Levavasseur, G., Lévy, C., Li, L., Lott, F., Lurton, T., Luyssaert, S., Madec, G., Madeleine, J.-B., Maignan, F., Marchand, M., Marti, O., Mellul, L., Meurdesoif, Y., Mignot, J., Musat, I., Ottlé, C., Peylin, P., Planton, Y., Polcher, J., Rio, C., Rochetin, N., Rousset, C., Sepulchre, P., Sima, A., Swingedouw, D., Thiéblemont, R., Traore, A. K., Vancoppenolle, M., Vial, J., Vialard, J., Viovy, N., and Vuichard, N.: Presentation and Evaluation of the IPSL-CM6A-LR Climate Model, J. Adv. Model. Earth Syst., 12, e2019MS002010, https://doi.org/10.1029/2019MS002010, 2020.

Brown, J.: Circum-Arctic Map of Permafrost and Ground-Ice Conditions. Version 2. Boulder, Colorado USA: National Snow and Ice Data Center., 2002.

Domine, F., Barrere, M., and Sarrazin, D.: Seasonal evolution of the effective thermal conductivity of the snow and the soil in high Arctic herb tundra at Bylot Island, Canada, The Cryosphere, 10, 2573–2588, https://doi.org/10.5194/tc-10-2573-2016, 2016.

Ducharne, A.: The hydrol module of ORCHIDEE: scientific documentation, 2018.

FAO, IIASA, ISRIC, ISSCAS and JRC: Harmonized WorldSoil Database (version 1.2), Tech. rep., FAO, Rome, Italy andIIASA, Laxenburg, Austria, 2012.

Gomis-Cebolla, J., Jimenez, J. C., and Sobrino, J. A.: LST retrieval algorithm adapted to the Amazon evergreen forests using MODIS data, Remote Sens. Environ., 204, 401–411, https://doi.org/10.1016/j.rse.2017.10.015, 2018.

https://doi.org/10.5194/gmd-2023-207
Preprint. Discussion started: 22 November 2023

655 Gouttevin, I., Menegoz, M., Domine, F., Krinner, G., Koven, C., Ciais, P., Tarnocai, C., and Boike, J.: How the insulating properties of snow affect soil carbon distribution in the continental pan-Arctic area, J. Geophys. Res. Biogeosciences, 117, 407-430, https://doi.org/10.1029/2011JG001916, 2012.

Guimberteau, M., Zhu, D., Maignan, F., Huang, Y., Yue, C., Dantec-Nédélec, S., Ottlé, C., Jornet-Puig, A., Bastos, A., Laurent, P., Goll, D., Bowring, S., Chang, J., Guenet, B., Tifafi, M., Peng, S., Krinner, G., Ducharne, A., Wang, F., Wang,
660 T., Wang, X., Wang, Y., Yin, Z., Lauerwald, R., Joetzjer, E., Qiu, C., Kim, H., and Ciais, P.: ORCHIDEE-MICT (v8.4.1), a land surface model for the high latitudes: model description and validation, Geosci. Model Dev., 11, 121–163, https://doi.org/10.5194/gmd-11-121-2018, 2018.

Hourdin, F.: Study and numerical simulation of the general circulation of planetary atmospheres, Ph.D. thesis, Paris VII University, 1992.

665 Hugelius, G., Tarnocai, C., Broll, G., Canadell, J. G., Kuhry, P., and Swanson, D. K.: The Northern Circumpolar Soil Carbon Database: spatially distributed datasets of soil coverage and soil carbon storage in the northern permafrost regions, Earth Syst Sci Data, 5, 3–13, https://doi.org/10.5194/essd-5-3-2013, 2013.

Hugelius, G., Strauss, J., Zubrzycki, S., Harden, J. W., Schuur, E. a. G., Ping, C.-L., Schirrmeister, L., Grosse, G., Michaelson, G. J., Koven, C. D., O'Donnell, J. A., Elberling, B., Mishra, U., Camill, P., Yu, Z., Palmtag, J., and Kuhry, P.:
670 Estimated stocks of circumpolar permafrost carbon with quantified uncertainty ranges and identified data gaps, Biogeosciences, 11, 6573–6593, https://doi.org/10.5194/bg-11-6573-2014, 2014.

Hugelius, G., Kuhry, P., and Tarnocai, C.: Ideas and perspectives: Holocene thermokarst sediments of the Yedoma permafrost region do not increase the northern peatland carbon pool, Biogeosciences, 13, 2003–2010, https://doi.org/10.5194/bg-13-2003-2016, 2016.

675 Hugelius, G., Loisel, J., Chadburn, S., Jackson, R. B., Jones, M., MacDonald, G., Marushchak, M., Olefeldt, D., Packalen, M., Siewert, M. B., Treat, C., Turetsky, M., Voigt, C., and Yu, Z.: Large stocks of peatland carbon and nitrogen are vulnerable to permafrost thaw, Proc. Natl. Acad. Sci., 117, 20438–20446, https://doi.org/10.1073/pnas.1916387117, 2020.

Koven, C., Friedlingstein, P., Ciais, P., Khvorostyanov, D., Krinner, G., and Tarnocai, C.: On the formation of high-latitude soil carbon stocks: Effects of cryoturbation and insulation by organic matter in a land surface model, Geophys. Res. Lett.,
680 36, https://doi.org/10.1029/2009GL040150, 2009.

Koven, C. D., Riley, W. J., Subin, Z. M., Tang, J. Y., Torn, M. S., Collins, W. D., Bonan, G. B., Lawrence, D. M., and Swenson, S. C.: The effect of vertically resolved soil biogeochemistry and alternate soil C and N models on C dynamics of CLM4, Biogeosciences, 10, 7109–7131, https://doi.org/10.5194/bg-10-7109-2013, 2013.

Krinner, G., Viovy, N., de Noblet-Ducoudré, N., Ogée, J., Polcher, J., Friedlingstein, P., Ciais, P., Sitch, S., and Prentice, I.
685 C.: A dynamic global vegetation model for studies of the coupled atmosphere-biosphere system, Glob. Biogeochem. Cycles, 19, GB1015, https://doi.org/10.1029/2003gb002199, 2005.

Lawrence, D. and Vandecar, K.: Effects of tropical deforestation on climate and agriculture, Nat. Clim. Change, 5, 27–36, https://doi.org/10.1038/nclimate2430, 2015.

https://doi.org/10.5194/gmd-2023-207
Preprint. Discussion started: 22 November 2023

Lawrence, D. M., Fisher, R. A., Koven, C. D., Oleson, K. W., Swenson, S. C., Bonan, G., Collier, N., Ghimire, B., van Kampenhout, L., Kennedy, D., Kluzek, E., Lawrence, P. J., Li, F., Li, H., Lombardozzi, D., Riley, W. J., Sacks, W. J., Shi, M., Vertenstein, M., Wieder, W. R., Xu, C., Ali, A. A., Badger, A. M., Bisht, G., van den Broeke, M., Brunke, M. A., Burns, S. P., Buzan, J., Clark, M., Craig, A., Dahlin, K., Drewniak, B., Fisher, J. B., Flanner, M., Fox, A. M., Gentine, P., Hoffman, F., Keppel-Aleks, G., Knox, R., Kumar, S., Lenaerts, J., Leung, L. R., Lipscomb, W. H., Lu, Y., Pandey, A., Pelletier, J. D., Perket, J., Randerson, J. T., Ricciuto, D. M., Sanderson, B. M., Slater, A., Subin, Z. M., Tang, J., Thomas, R. Q., Val Martin, M., and Zeng, X.: The Community Land Model Version 5: Description of New Features, Benchmarking, and Impact of Forcing Uncertainty, J. Adv. Model. Earth Syst., 11, 4245–4287, https://doi.org/10.1029/2018MS001583, 2019.

Li, H., Sun, D., Yu, Y., Wang, H., Liu, Y., Liu, Q., Du, Y., Wang, H., and Cao, B.: Evaluation of the VIIRS and MODIS LST products in an arid area of Northwest China, Remote Sens. Environ., 142, 111–121, https://doi.org/10.1016/j.rse.2013.11.014, 2014.

Li, Y., Zhao, M., Motesharrei, S., Mu, Q., Kalnay, E., and Li, S.: Local cooling and warming effects of forests based on satellite observations, Nat. Commun., 6, 6603, https://doi.org/10.1038/ncomms7603, 2015.

Li, Y., Brando, P. M., Morton, D. C., Lawrence, D. M., Yang, H., and Randerson, J. T.: Deforestation-induced climate change reduces carbon storage in remaining tropical forests, Nat. Commun., 13, 1964, https://doi.org/10.1038/s41467-022-29601-0, 2022.

Lindgren, A., Hugelius, G., and Kuhry, P.: Extensive loss of past permafrost carbon but a net accumulation into present-day soils, Nature, 560, 219–222, https://doi.org/10.1038/s41586-018-0371-0, 2018.

Melton, J. R. and Arora, V. K.: Sub-grid scale representation of vegetation in global land surface schemes: implications for estimation of the terrestrial carbon sink, Biogeosciences, 11, 1021–1036, https://doi.org/10.5194/bg-11-1021-2014, 2014.

Melton, J. R., Arora, V. K., Wisernig-Cojoc, E., Seiler, C., Fortier, M., Chan, E., and Teckentrup, L.: CLASSIC v1.0: the open-source community successor to the Canadian Land Surface Scheme (CLASS) and the Canadian Terrestrial Ecosystem Model (CTEM) – Part 1: Model framework and site-level performance, Geosci. Model Dev., 13, 2825–2850, https://doi.org/10.5194/gmd-13-2825-2020, 2020.

Obu, J., Westermann, S., Bartsch, A., Berdnikov, N., Christiansen, H. H., Dashtseren, A., Delaloye, R., Elberling, B., Etzelmüller, B., Kholodov, A., Khomutov, A., Kääb, A., Leibman, M. O., Lewkowicz, A. G., Panda, S. K., Romanovsky, V., Way, R. G., Westergaard-Nielsen, A., Wu, T., Yamkhin, J., and Zou, D.: Northern Hemisphere permafrost map based on TTOP modelling for 2000–2016 at 1 km2 scale, Earth-Sci. Rev., 193, 299–316, https://doi.org/10.1016/j.earscirev.2019.04.023, 2019.

Palmtag, J., Obu, J., Kuhry, P., Richter, A., Siewert, M. B., Weiss, N., Westermann, S., and Hugelius, G.: A high spatial resolution soil carbon and nitrogen dataset for the northern permafrost region based on circumpolar land cover upscaling, Earth Syst. Sci. Data, 14, 4095–4110, https://doi.org/10.5194/essd-14-4095-2022, 2022.

https://doi.org/10.5194/gmd-2023-207
Preprint. Discussion started: 22 November 2023

Peng, S., Piao, S., Zeng, Z., Ciais, P., Zhou, L., Li, L. Z. X., Myneni, R. B., Yin, Y., and Zeng, H.: Afforestation in China cools local land surface temperature, Proc. Natl. Acad. Sci., 111, 2915–2919, https://doi.org/10.1073/pnas.1315126111, 2014.

Peng, S., Ciais, P., Krinner, G., Wang, T., Gouttevin, I., McGuire, A. D., Lawrence, D., Burke, E., Chen, X., Decharme, B., Koven, C., MacDougall, A., Rinke, A., Saito, K., Zhang, W., Alkama, R., Bohn, T. J., Delire, C., Hajima, T., Ji, D., Lettenmaier, D. P., Miller, P. A., Moore, J. C., Smith, B., and Sueyoshi, T.: Simulated high-latitude soil thermal dynamics during the past 4 decades, The Cryosphere, 10, 179–192, https://doi.org/10.5194/tc-10-179-2016, 2016.

Qiu, C., Zhu, D., Ciais, P., Guenet, B., Krinner, G., Peng, S., Aurela, M., Bernhofer, C., Brümmer, C., Bret-Harte, S., Chu, H., Chen, J., Desai, A. R., Dušek, J., Euskirchen, E. S., Fortuniak, K., Flanagan, L. B., Friborg, T., Grygoruk, M., Gogo, S., Grünwald, T., Hansen, B. U., Holl, D., Humphreys, E., Hurkuck, M., Kiely, G., Klatt, J., Kutzbach, L., Largeron, C., Laggoun-Défarge, F., Lund, M., Lafleur, P. M., Li, X., Mammarella, I., Merbold, L., Nilsson, M. B., Olejnik, J., Ottosson-Löfvenius, M., Oechel, W., Parmentier, F. J. W., Peichl, M., Pirk, N., Peltola, O., Pawlak, W., Rasse, D., Rinne, J., Shaver, G., Schmid, H. P., Sottocornola, M., Steinbrecher, R., Sachs, T., Urbaniak, M., Zona, D., and Ziemblinska, K.: ORCHIDEE-PEAT (revision 4596), a model for northern peatland CO2, water, and energy fluxes on daily to annual scales, Geosci. Model Dev., 11, 497–519, https://doi.org/10.5194/gmd-11-497-2018, 2018.

Qiu, C. J., Zhu, D., Ciais, P., Guenet, B., Peng, S. S., Krinner, G., Tootchi, A., Ducharne, A., and Hastie, A.: Modelling northern peatland area and carbon dynamics since the Holocene with the ORCHIDEE-PEAT land surface model (SVN r5488), Geosci. Model Dev., 12, 2961–2982, https://doi.org/10.5194/gmd-12-2961-2019, 2019.

Ramdane Alkama and Alessandro Cescatti: Biophysical climate impacts of recent changes in global forest cover, Science, 351, 600–604, https://doi.org/doi:10.1126/science.aac8083, 2016.

Rumbold, H. S., Gilham, R. J. J., and Best, M. J.: Assessing methods for representing soil heterogeneity through a flexible approach within the Joint UK Land Environment Simulator (JULES) at version 3.4.1, Geosci. Model Dev., 16, 1875–1886, https://doi.org/10.5194/gmd-16-1875-2023, 2023.

Sherstiukov, A.: Statistical quality control of soil temperature dataset, RIHMI-WDC, 176, 224–232, 2012.

Su, Y., Zhang, C., Ciais, P., Zeng, Z., Cescatti, A., Shang, J., Chen, J. M., Liu, J., Wang, Y.-P., Yuan, W., Peng, S., Lee, X., Zhu, Z., Fan, L., Liu, X., Liu, L., Lafortezza, R., Li, Y., Ren, J., Yang, X., and Chen, X.: Asymmetric influence of forest cover gain and loss on land surface temperature, Nat. Clim. Change, 13, 823–831, https://doi.org/10.1038/s41558-023-01757-7, 2023.

Wan, Z.: Collection-6 MODIS Land Surface Temperature ProductsUsers' Guide, Earth Research Institute, University of California,Santa Barbara, 2013.

Wan, Z.: New refinements and validation of the collection-6 MODIS land-surface temperature/emissivity product, Remote Sens. Environ., 140, 36–45, https://doi.org/10.1016/j.rse.2013.08.027, 2014.

Wang, T., Ottlé, C., Boone, A., Ciais, P., Brun, E., Morin, S., Krinner, G., Piao, S., and Peng, S.: Evaluation of an improved intermediate complexity snow scheme in the ORCHIDEE land surface model, J. Geophys. Res. Atmospheres, 118, 6064–6079, https://doi.org/10.1002/jgrd.50395, 2013.

Westermann, S., Langer, M., and Boike, J.: Systematic bias of average winter-time land surface temperatures inferred from MODIS at a site on Svalbard, Norway, Remote Sens. Environ., 118, 162–167, https://doi.org/10.1016/j.rse.2011.10.025, 2012.

Wu, Y., Xi, Y., Feng, M., and Peng, S.: Wetlands Cool Land Surface Temperature in Tropical Regions but Warm in Boreal Regions, Remote Sens., 13, 1439, https://doi.org/10.3390/rs13081439, 2021.

Xi, Y.: Code for GMD paper: Assessment of a multi-tiling energy budget approach in a land surface model, ORCHIDEE-MICT (r8205). Zenodo. https://doi.org/10.5281/zenodo.10014533, 2023.

Xu, J., Morris, P., Liu, J., and Holden, J.: PEATMAP: Refining estimates of global peatland distribution based on a meta-analysis, Catena, 160, 134–140, https://doi.org/10.1016/j.catena.2017.09.010, 2018.

Zhang, T.: Influence of the seasonal snow cover on the ground thermal regime: An overview, Rev. Geophys., 43, https://doi.org/10.1029/2004RG000157, 2005.

Zhu, D., Peng, S. S., Ciais, P., Viovy, N., Druel, A., Kageyama, M., Krinner, G., Peylin, P., Ottle, C., Piao, S. L., Poulter, B., Schepaschenko, D., and Shvidenko, A.: Improving the dynamics of Northern Hemisphere high-latitude vegetation in the ORCHIDEE ecosystem model, Geosci. Model Dev., 8, 2263–2283, https://doi.org/10.5194/gmd-8-2263-2015, 2015.

Zhu, D., Peng, S., Ciais, P., Zech, R., Krinner, G., Zimov, S., and Grosse, G.: Simulating soil organic carbon in yedoma deposits during the Last Glacial Maximum in a land surface model, Geophys. Res. Lett., 43, 5133–5142, https://doi.org/10.1002/2016GL068874, 2016.

Zhu, D., Ciais, P., Krinner, G., Maignan, F., Jornet Puig, A., and Hugelius, G.: Controls of soil organic matter on soil thermal dynamics in the northern high latitudes, Nat. Commun., 10, 3172, https://doi.org/10.1038/s41467-019-11103-1, 2019.

Zhu, L., Li, W., Ciais, P., He, J., Cescatti, A., Santoro, M., Tanaka, K., Cartus, O., Zhao, Z., Xu, Y., Sun, M., and Wang, J.: Comparable biophysical and biogeochemical feedbacks on warming from tropical moist forest degradation, Nat. Geosci., 16, 244–249, https://doi.org/10.1038/s41561-023-01137-y, 2023.